




Applied Computational
Electromagnetics Society



Newsletter
Volume 22 – No. 2
ISSN 1056-9170



July 2007



**APPLIED COMPUTATIONAL ELECTROMAGNETICS SOCIETY
(ACES)**

NEWSLETTER

Vol. 22 No. 2

July 2007

TABLE OF CONTENTS

ANNOUNCEMENT	
New Newsletter Editor-in-Chief	6
PERSPECTIVES IN CEM	
“So far, so good?”	
Alistair Duffy	7
TECHNICAL FEATURE ARTICLE	
“New Basis Functions for the Electromagnetic Solution of Arbitrarily-shaped, Three dimensional Conducting Bodies Using Method of Moments	
Anne I. Mackenzie, Michael E. Baginski, Sadasiva M. Rao	10
TUTORIAL	
“Computational Electromagnetic Field Calculation by means of Finite Integration Technique (FIT) and/or Method of Moment (MoM)”	
A.Ciccomancini Scogna, M. Strydom.....	17
TECHNICAL ARTICLE	
“Exact Radiation by Isorefractive Slotted Elliptic Cylindrical Antenna”	
A-K. Hamid, M.I. Hussein, M. Hamid	42
ANNOUNCEMENTS:	
ADVERTISING Rates	58
DEADLINE for Submission of Articles.....	58
Last Word	58

PERMANENT STANDING COMMITTEES OF ACES, INC.
--

COMMITTEE	CHAIRMAN	ADDRESS
NOMINATION	Rene Allard	Penn State University PO Box 30 State College, PA 16804-0030 rja5@psu.edu
ELECTIONS	Rene Allard	Penn State University PO Box 30 State College, PA 16804-0030 rja5@psu.ed
FINANCE	Andrew Peterson	Georgia Institute of Technology School of ECE Atlanta, GA 30332-0250 peterson@ece.gatech.edu
PUBLICATIONS	Atef Elsherbeni	EE Department, Anderson Hall University of Mississippi University, MS 38677 atef@olemiss.edu
CONFERENCE	Osama Mohammed	Florida International University ECE Department Miami, FL 33174 mohammed@fiu.edu
AWARDS	Ray Perez	Martin Marietta Astronautics MS 58700, PO Box 179 Denver, CO 80201 ray.j.perez@lmco.com

MEMBERSHIP ACTIVITY COMMITTEES OF ACES, INC.

COMMITTEE	CHAIRMAN	ADDRESS
SOFTWARE VALIDATION	Bruce Archambeault	IBM 3039 Cornwallis Road, PO Box 12195 Dept. 18DA B306 Research Triangle Park NC 27709
HISTORICAL	(Vacant)	
CONSTITUTION & BYLAWS	Leo Kempel	2120 Engineering Building Michigan State University East Lansing, MI 48824 kempel@egr.msu.edu
MEMBERSHIP & COMMUNICATIONS	Vicente Rodriguez	ETS-LINDGREN L.P. 1301 Arrow Point Drive Cedar Park, TX 78613 rodriguez@ieee.org
INDUSTRIAL RELATIONS	Andy Drozd	ANDRO Consulting Services PO Box 543 Rome, NY 13442-0543 Andro1@aol.com

ACES NEWSLETTER STAFF

EDITOR-IN-CHIEF, NEWSLETTER

Bruce Archambeault
IBM
3039 Cornwallis Road, PO Box 12195
Dept. 18DA B306
Research Triangle Park, NC 27709
Phone: 919-486-0120
email: barch@us.ibm.com

EDITOR-IN-CHIEF, PUBLICATIONS

Atef Elsherbeni
EE Department, Anderson Hall
University of Mississippi
University, MS 38677
Email: atef@olemiss.edu

ASSOCIATE EDITOR-IN-CHIEF

Ray Perez
Martin Marietta Astronautics
MS 58700, PO Box 179
Denver, CO 80201
Phone: 303-977-5845
Fax: 303-971-4306
email: ray.j.perez@lmco.com

MANAGING EDITOR

Richard W. Adler
Naval Postgraduate School/ECE Dept.
Code ECAB, 833 Dyer Road,
Monterey, CA 93943-5121
Fax: 831-649-0300
Phone: 831-646-1111
email: rwa@att.biz

EDITORS

CEM NEWS FROM EUROPE

Tony Brown
University of Manchester
PO Box 88 Sackville Street
Manchester M60 1QD United Kingdom
Phone: +44 (0) 161-200-4779
Fax: +44 (0) 161-200-8712
email: Anthony.brown@manchester.ac.uk

TECHNICAL FEATURE ARTICLE

Andy Drodz
ANDRO Consulting Services
PO Box 543
Rome, NY 13442-0543
Phone: 315-337-4396
Fax: 314-337-4396
email: androl@aol.com

THE PRACTICAL CEMIST

W. Perry Wheless, Jr.
University of Alabama
PO Box 11134
Tuscaloosa, AL 35486-3008
Phone: 205-348-1757
Fax: 205-348-6959
email: wwheless@coe.eng.ua.edu

MODELER'S NOTES

Gerald Burke
Lawrence Livermore National Labs.
Box 5504/L-156
Livermore, CA 94550
Phone: 510-422-8414
Fax: 510-422-3013
email: burke2@llnl.gov

PERSPECTIVES IN CEM

Alistair Duffy
School of Engineering and Technology
De Montfort University
The Gateway
Leicester, UK LE1 9BH
+44(0)116 257 7056
apd@dmu.ac.uk

TUTORIAL

Giulio Antonini
UAq EMC Laboratory
Department of Electrical Engineering
University of L'Aquila
Poggio di Roio, 67040 Italy
Phone: +39-0862-43446
email: antonini@ing.univaq.it

ACES JOURNAL

EDITOR IN CHIEF

Atef Elsherbeni
Associate Editor-in-Chief Journal, Alexander Yakovlev
EE Department, Anderson Hall
University of Mississippi
University, MS 38677
Phone: 662-915-5382
email: atef@olemiss.edu

NEWSLETTER ARTICLES AND VOLUNTEERS WELCOME

The ACES Newsletter is always looking for articles, letters and short communications of interest to ACES members. All individuals are encouraged to write, suggest or solicit articles either on a one-time or continuing basis. Please contact a Newsletter Editor.

AUTHORSHIP AND BERNE COPYRIGHT CONVENTION

The opinions, statements and facts contained in this Newsletter are solely the opinions of the authors and/or sources identified with each article. Articles with no author can be attributed to the editors or to the committee head in the case of committee reports. The United States recently became part of the Berne Copyright Convention. Under the Berne Convention, the copyright for an article in this newsletter is legally held by the author(s) of the article since no explicit copyright notice appears in the newsletter.

BOARD OF DIRECTORS					
EXECUTIVE COMMITTEE					
Osama Mohammed, President		Allen W. Glisson, Treasurer			
Atef Elsherbeni, Vice President		Richard W. Adler, Executive Officer			
Leo Kemple, Secretary					
DIRECTORS-AT-LARGE					
Randy Haupt	2007	Atef Elsherbeni	2008	C.J. Reddy	2009
Juan Mosig	2007	Michiko Kuroda	2008	Osama Mohammed	2009
Allen Glisson	2007	Eric Mokole	2008	Natalia Nikolova	2009

ACES ELECTRONIC PUBLISHING GROUP	
Atef Elsherbeni	Electronic Publishing Managing Editor
Matthew J. Inman	Site Administrator
Mohamed Al Sharkawy	Contributing Staff
Imran Kader	Past Site Administrator
Orin H. Council	Past Staff
Brad Baker	Past Staff
Jessica Drewrey	Past Staff
Chris Riley	Past Staff
Visit us on line at: http://aces.ee.olemiss.edu	

Announcement

This is my last ACES Newsletter issue as Editor-in-Chief. The good news is that Alistair Duffy has agreed to take over as Editor-in-Chief. You all know him as the Editor for Perspectives, and he has written some very interesting and thought provoking articles for that section.

I have enjoyed working with the entire staff of the Newsletter, and without all their help, there would be *no* Newsletter. I wish to give a special thanks to Dick Adler who has put the final touches on each and every issue, and has corrected more mistakes than I would like to admit to making!

I have been the Newsletter Editor-in-Chief for over four years. Recent additional responsibilities at IBM have made it very difficult to continue in this role because of time constraints. I know that Alistair will bring a renewed enthusiasm to the Newsletter, and I look forward to seeing the new issues.

Please feel free to contact me at any time. I plan to continue to be an active ACES member and I'll see you at the yearly ACES conference!

Sincerely

Bruce Archambeault
barch@us.ibm.com

So far, so good?

Dr Alistair Duffy
apd@dmu.ac.uk

“Perspectives in CEM” has been running for a few issues in the current form. I thought it would be appropriate to provide a brief recap of the themes that have been developed. Why do this? Some of the following issues will be written by other people and a review here might serve to encourage more personal perspectives. So if you have opinions, views, experience or observations on these (or other) topics that you would like to share with the rest of the ACES community, please contact me.

Electromagnetics Education

“A New Modelling Army” and “The Lives of Subjects” asked whether we should turn the traditional method of teaching electromagnetics on its head and, effectively, leave an understanding of the mathematical basis of electromagnetics until a later stage in an undergraduate course. The result of doing this could be that there will be more engineers able to drive packages without having the detailed mathematical understanding. A conclusion was that

“Should we concentrate on developing practical skills, first, in the many and mathematical skills later in the few? Perhaps it is time to move on, and concentrate on ensuring that more students have skills in doing the basics, such as simulating and visualising field behaviour and are able to identify when something is ‘not quite right’ or understand the basic limitations of their chosen modeling approach. Of those that get beyond a general understanding of fields, they can be more formally educated with a strong mathematical and analytical understanding. In doing this our New Modelling Army will be well trained, well organised and the discipline itself will be well constructed. Hopefully, our Ironsides will be well and regularly paid and will be able cast their influence widely and for a long time.”

‘Good Enough’ Modeling

“Satisficing in Computational Electromagnetics” and “Keep it Simple” were based on a straightforward proposition:

Where time issues are important in simulations, we do not generally need to strive for fine resolution and high accuracy. In many cases, the questions being answered through modelling can be best addressed by ‘sub-optimal’ models which deliver acceptable results in an acceptable time using an acceptable platform.

An approach to achieving a satisfied, or good enough, result was suggested:

- 1. Consider what the goals of the activity (experiment, simulation) are.*
- 2. Determine the range of parameters and associated collection of values that must be met for those goals to be satisfied.*
- 3. Use “Five Whys” to explore these reasons in depth.*
- 4. Iteratively create models and dry-run them to see if they meet the constraints, on a "Go"/"No Go" basis before proceeding with the actual simulation.*

The idea of not using any more detail than you need to has been around for over half a millennium yet it is not uncommon for modelers to get quite upset if assumptions and presence of errors are accepted *a priori* and their precision tool is being used in an imprecise way.

Peer review

“Anonymous Peer Review. Time To Move On?” asked whether we should move more open peer reviewing rather than continuing with anonymous peer review. It discussed three points:

- 1. Anonymity allows referees to say what they really think about a paper. Promoting objectivity.***
- 2. If you are not prepared to put your name to a comment, should you really make it? Promoting ethical reviewing.***
- 3. Misunderstandings are human and often resolved through dialogue. Promoting the communication of science.***

One question that was implied by this article was whether we are tied into anonymous peer review largely because that is the way it has always been done in our community.

This “Perspectives” has taken some, but not all, of the themes that have been discussed over the last couple of years and tried to capture some of the main points being raised in them. Please feel free to vehemently disagree with anything I have said, passionately support it, or just ask more questions. I would like to invite anyone in the ACES community reading this to have your say, put across your perspective on any of the above themes or just share your experiences.

Comprehensive
Electromagnetic
Solutions



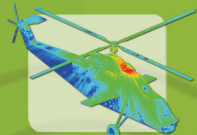
Where ideas are brought to life!



- UTD
- PO
- GO
- MLFMM
- FEM/MoM

3D EM SIMULATION SOFTWARE

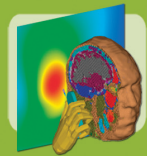
for real life problems, with FREE 45 days evaluation



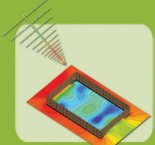
Antenna Placement



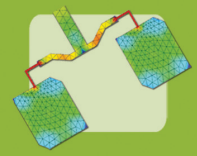
Antenna Design



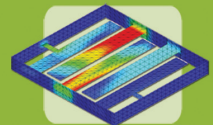
Dielectric Bodies



EMC



Microstrip Antennas



Stripline & Circuits

www.feko.info

New Basis Functions for the Electromagnetic Solution of Arbitrarily-shaped, Three Dimensional Conducting Bodies Using Method of Moments

Anne I. Mackenzie¹, Michael E. Baginski², Sadasiva M. Rao³

¹NASA Langley Research Center, Hampton, VA 23681 (USA), email:anne.mackenzie-1@nasa.gov

²Department of E & CE, Auburn University, Auburn, AL 36849 (USA), email:baginme@auburn.edu

³Department of E & CE, Auburn University, Auburn, AL 36849 (USA), email:rao@eng.auburn.edu

Abstract

In this work, we present a new set of basis functions, defined over a pair of planar triangular patches, for the solution of electromagnetic scattering and radiation problems associated with arbitrarily-shaped surfaces using the method of moments solution procedure. The basis functions are constant over the function subdomain and resemble pulse functions for one and two dimensional problems. Further, another set of basis functions, point-wise orthogonal to the first set, is also defined over the same function space. The primary objective of developing these basis functions is to utilize them for the electromagnetic solution involving conducting, dielectric, and composite bodies. However, in the present work, only the conducting body solution is presented and compared with other data.

1 Introduction

The solution of electromagnetic scattering/radiation problems involving arbitrary shapes and material composition is of much interest to commercial as well as defense industries. The method of moments (MoM) [1] solutions to these problems generally involve triangular patch modeling and utilizing Rao-Wilton-Glisson (RWG) basis functions [2]. It may be noted that the RWG basis functions have been primarily defined for the solution of conducting bodies and the utilization of the same basis functions for dielectric/composite bodies is less than satisfactory. The primary difficulty associated with a material body solution is the requirement of two orthogonal basis functions to express unknown electric and magnetic currents \mathbf{J} and \mathbf{M} . In our opinion, using the same basis functions for both \mathbf{J} and \mathbf{M} is not a good idea and invariably results in numerical difficulties. However, a host of techniques have been developed which involve either tinkering with the basis functions or modifying the testing procedures to apply to material bodies [3, 4, 5]. Keeping these difficulties in perspective, in this work, we present two sets of basis functions, each one point-wise orthogonal to the other function, which can be used for conducting as well as material bodies. The present work, however, involves only conducting bodies along with several numerical results. The solution of the material body problem will be presented in a future article.

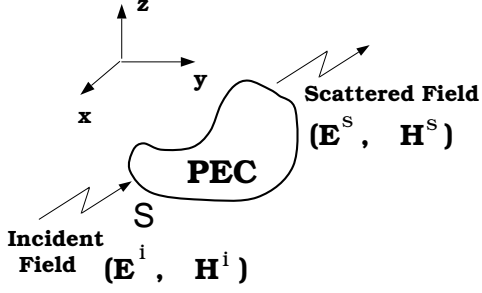


Figure 1: Arbitrarily-shaped conducting body excited by an incident electromagnetic plane wave.

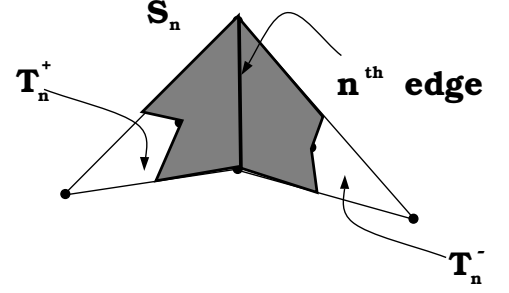


Figure 2: Basis function description.

2 Description of the Problem

Let S denote the surface of an arbitrarily-shaped perfectly conducting body illuminated by an incident electromagnetic plane wave \mathbf{E}^i as shown in Figure 1. Using the equivalence principle, potential theory and the free-space Green's function [1], the electric field integral equation (EFIE) is given by

$$[j\omega\mathbf{A} + \nabla\Phi]_{tan} = \mathbf{E}_{tan}^i \quad (1)$$

where the subscript “tan” refers to the tangential component. In (1),

$$\mathbf{A} = \mu \int_S \mathbf{J}_s G ds' \quad (2)$$

$$\Phi = \epsilon^{-1} \int_S q_s G ds' \quad (3)$$

$$G = \frac{e^{-jkR}}{4\pi R} \quad (4)$$

$$R = |\mathbf{r} - \mathbf{r}'| \quad (5)$$

ϵ and μ are permittivity and permeability of the surrounding medium, k is the wave number and \mathbf{r} and \mathbf{r}' represent the position vectors to observation and source points, respectively, from a global coordinate origin. The unknown surface current \mathbf{J}_s is related to the charge density q_s by the continuity equation, given by

$$\nabla \bullet \mathbf{J}_s = -j\omega q_s \quad (6)$$

For the numerical solution of (1), we apply the method of moments formulation using planar triangular patch modeling and the basis functions as described in the following section:

3 Description of Basis Functions

Let T_n^+ and T_n^- represent two triangles connected to the edge n of the triangulated surface model as shown in Figure 2. We define two mutually orthogonal vector basis functions associated with the n^{th} edge as

$$\mathbf{f}_n(\mathbf{r}) = \begin{cases} \mathbf{a}_n^\pm \times \hat{\boldsymbol{\ell}}, & \mathbf{r} \in S_n, \\ 0, & \text{otherwise} \end{cases} \quad (7)$$

and

$$\mathbf{g}_n(\mathbf{r}) = \begin{cases} \hat{\boldsymbol{\ell}}, & \mathbf{r} \in S_n, \\ 0, & \text{otherwise} \end{cases} \quad (8)$$

where S_n represents the region obtained by connecting the mid-points of the free edges to the centroids of triangles T_n^\pm , and to the nodes of edge n . Note that this area is shown shaded in the Figure 2. Also, $\hat{\boldsymbol{\ell}}$ and \mathbf{a}_n^\pm represent the unit vector along the n^{th} edge and the unit normal vector to the plane of the triangle T_n^\pm , respectively. Note that the basis functions defined in (8) are actually the pulse functions defined over the region S_n . It is well-known that the pulse functions do not have continuous derivatives but result in delta distributions along the boundary. This point is crucial in modeling the charge density and the calculation of scalar potential which may be accomplished as described in the following section. Also, note that in this work, only perfect electric conductor (PEC) bodies are analyzed and hence only \mathbf{f}_n 's are used in the method of moments solution.

4 Numerical Solution Procedure

As a first step, we consider the testing procedure. Consider the m^{th} interior edge, associated with triangles T_m^\pm . We integrate the vector component of (1) parallel to the path from the centroid \mathbf{r}_m^{c+} of T_m^+ , to the midpoint of the edge \mathbf{r}_m and thence from \mathbf{r}_m to the centroid of T_m^- given by \mathbf{r}_m^{c-} . For both path integrations, approximate \mathbf{A} and \mathbf{E}^i by their respective values at the mid-points of each path. Thus, we have,

$$\begin{aligned} j\omega\mathbf{A}\left(\frac{\mathbf{r}_m + \mathbf{r}_m^{c+}}{2}\right) \bullet (\mathbf{r}_m - \mathbf{r}_m^{c+}) + j\omega\mathbf{A}\left(\frac{\mathbf{r}_m + \mathbf{r}_m^{c-}}{2}\right) \bullet (\mathbf{r}_m^{c-} - \mathbf{r}_m) + \\ [\Phi(\mathbf{r}_m^{c-}) - \Phi(\mathbf{r}_m^{c+})] = \mathbf{E}^i\left(\frac{\mathbf{r}_m + \mathbf{r}_m^{c+}}{2}\right) \bullet (\mathbf{r}_m - \mathbf{r}_m^{c+}) + \\ \mathbf{E}^i\left(\frac{\mathbf{r}_m + \mathbf{r}_m^{c-}}{2}\right) \bullet (\mathbf{r}_m^{c-} - \mathbf{r}_m) \end{aligned} \quad (9)$$

for $m = 1, 2, \dots, N$, where N represents the total number of interior edges in the triangulation scheme, *i.e.* excluding the edges on the boundary for an open body.

Next, we consider the expansion procedure. Using the basis functions \mathbf{f}_n defined in (8), we approximate the unknown current \mathbf{J} as

$$\mathbf{J} = \sum_{n=1}^N I_n \mathbf{f}_n \quad (10)$$

Next, substituting the current expansion (10) into (9) yields an $N \times N$ system of linear equations which may be written in matrix form as $\mathbf{Z}\mathbf{I} = \mathbf{V}$, where $\mathbf{Z} = [Z_{mn}]$ is an $N \times N$ matrix and $\mathbf{I} = [I_n]$ and $\mathbf{V} = [V_m]$ are column vectors of length N . The elements of the \mathbf{Z} and \mathbf{V} are given by

$$Z_{mn} = j\omega \left[\mathbf{A}_{mn}^+ \bullet (\mathbf{r}_m - \mathbf{r}_m^{c+}) + \mathbf{A}_{mn}^- \bullet (\mathbf{r}_m^{c-} - \mathbf{r}_m) \right] + \Phi_{mn}^- - \Phi_{mn}^+ \quad (11)$$

$$V_m = \mathbf{E}_m^+ \bullet (\mathbf{r}_m - \mathbf{r}_m^{c+}) + \mathbf{E}_m^- \bullet (\mathbf{r}_m^{c-} - \mathbf{r}_m) \quad (12)$$

where

$$\mathbf{A}_{mn}^\pm = \mu \int_S \mathbf{f}_n \frac{e^{-jkR_m^\pm}}{4\pi R_m^\pm} dS' \quad (13)$$

$$\Phi_{mn}^\pm = \frac{-1}{j\omega\epsilon} \int_S \nabla_s \bullet \mathbf{f}_n \frac{e^{-jkR_m^{c\pm}}}{4\pi R_m^{c\pm}} dS' \quad (14)$$

$$R_m^\pm = \left| \frac{\mathbf{r}_m + \mathbf{r}_m^{c\pm}}{2} - \mathbf{r}' \right| \quad (15)$$

$$R_m^{c\pm} = |\mathbf{r}_m^{c\pm} - \mathbf{r}'| \quad (16)$$

$$\mathbf{E}_m^\pm = \mathbf{E}^i \left(\frac{\mathbf{r}_m + \mathbf{r}_m^{c\pm}}{2} \right) \quad (17)$$

The numerical evaluation of the vector potential, shown in (13), is straightforward and may be accomplished by the procedure described in [6]. However, the numerical evaluation of the scalar potential term, described in (14), may be carried out as follows:

Let us define the unknown charge density q_s in (3), as

$$q_s = \sum_{i=1}^{N_P} \alpha_i P_i \quad (18)$$

where N_P represents the number of triangular patches in the model, α_i is the unknown coefficient, and

$$P_i(\mathbf{r}) = \begin{cases} 1, & \mathbf{r} \in T_i \\ 0, & \text{otherwise} \end{cases} \quad (19)$$

Next, consider a triangular patch T_i with associated non-boundary edges, i_1 , i_2 , and i_3 . Then, using (6), the well-known Divergence theorem, and simple vector calculus, we have

$$\begin{aligned} \int_{T_i} q_s ds &= \int_{T_i} \frac{\nabla_s \bullet \mathbf{J}}{-j\omega} ds \\ &= \frac{j}{\omega} \oint_{C_i} \mathbf{J} \bullet \mathbf{n}_\ell d\ell \\ &= \frac{j}{\omega} [I_{i_1} \ell_{i_1} + I_{i_2} \ell_{i_2} + I_{i_3} \ell_{i_3}] \end{aligned} \quad (20)$$

where C_i is the contour bounding the triangle T_i , \mathbf{n}_ℓ is the unit normal vector to the contour C_i in the plane of T_i , and $\ell_{i_j}, j = 1, 2, 3$ represent the edge lengths. Also, note that

$$\begin{aligned} \int_{T_i} q_s ds &= \int_{T_i} \alpha_i ds \\ &= \alpha_i A_i \end{aligned} \quad (21)$$

where A_i represents the area of the triangle T_i . Lastly, using (20) and (21), we have

$$\alpha_i = \frac{j}{\omega} \left[\frac{I_{i_1} \ell_{i_1} + I_{i_2} \ell_{i_2} + I_{i_3} \ell_{i_3}}{A_i} \right] \quad (22)$$

Thus, we can write the scalar potential term in (14) as,

$$\Phi_{mn}^\pm = \frac{j\ell_n}{\omega\epsilon} \left[\frac{1}{A_{n^+}} \int_{T_n^+} \frac{e^{-jkR_m^{c\pm}}}{4\pi R_m^{c\pm}} dS' - \frac{1}{A_{n^-}} \int_{T_n^-} \frac{e^{-jkR_m^{c\pm}}}{4\pi R_m^{c\pm}} dS' \right] \quad (23)$$

Finally, once the matrices \mathbf{Z} and \mathbf{V} are determined, one may easily solve the system of linear equations to obtain \mathbf{I} .

5 Numerical Results

In this section, we present numerical results for a square plate (length = 0.15λ), circular disk (diameter = 0.15λ), a sphere (diameter = 0.15λ) and a circular cylinder (diameter = 0.15λ , length = 0.15λ), and compare with the solution obtained using the procedure presented in [2]. Also, for the case of the sphere, the results are compared with the exact solution. The plate, the disk, the sphere, and the cylinder are modeled with 312, 258, 500, and 320 triangles, respectively. In every case, the body is placed at the center of the coordinate system and illuminated by an x-polarized plane wave traveling along the z-axis. Further, the square plate and the circular disk are oriented parallel to the xy-plane. The bistatic radar cross section (RCS) is presented in figures 3, 4, 5, and 6. We note that the results compare well with the other numerical results.

6 Conclusions

In this work, we present a new set of basis functions for the method of moments solution of electromagnetic scattering by conducting bodies of arbitrary shape. The new basis functions are pulse basis functions defined over a pair of triangular patches. Another set of basis functions, point-wise orthogonal to the first set, is also presented. It is hoped that these two sets of basis functions, in conjunction with the method of moments solution procedure, provide a more stable solution to material problems. However, in the present work, only conducting scatterers are analyzed with the new basis functions and the results are compared with those from other solution methods. At present, the work is in progress to apply the new basis functions to material bodies and will be reported in the future.

References

- [1] R. F. Harrington, *Time-Harmonic Electromagnetic Fields*, New York, McGraw-Hill, 1961.
- [2] S. M. Rao, D. R. Wilton, and A. W. Glisson, "Electromagnetic Scattering by Surfaces of Arbitrary Shape", *IEEE Transactions on Antennas and Propagation*, Vol. 30, pp. 409 - 418, 1982.
- [3] S. M. Rao and D. R. Wilton, "E-field, H-field, and Combined Field Solution for Arbitrary Shaped Three Dimensional Dielectric Objects", *Electromagnetics*, vol. 10, pp. 407 - 421, October - December 1990.
- [4] S. M. Rao, T. K. Sarkar, P. Midya, and A. R. Djordjevic, "Electromagnetic Scattering from Finite Conducting and Dielectric Structures : Surface/Surface Formulation", *IEEE Transactions Antennas and Propagation*, vol. 39, pp. 1034 - 1037, July 1991.
- [5] X. Q. Sheng, J. M. Jin, J. Song, W. C. Chew, C. C. Lu, "Solution of combined-field integral equation using multilevel fast multipole algorithm for scattering by homogeneous bodies", *IEEE Transactions Antennas and Propagation*, vol. 46, pp. 1718 - 1726, November 1998.
- [6] D. R. Wilton, S. M. Rao, A. W. Glisson, D. H. Schaubert, O. M. Al-Bundak, and C. M. Butler, "Potential Integrals for Uniform and Linear Source Distributions on Polygonal and Polyhedral Domains ", *IEEE Transactions on Antennas and Propagation*, vol. 32, pp. 276 - 281, March 1984.

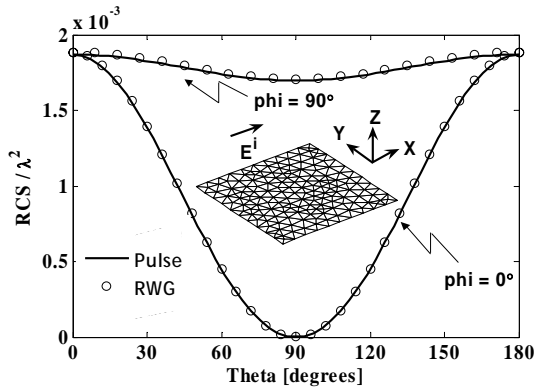


Figure 3: Bistatic RCS of a square plate.

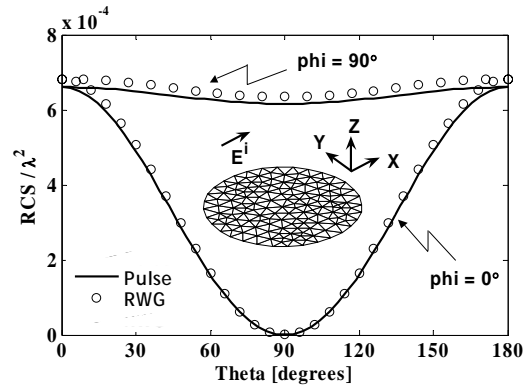


Figure 4: Bistatic RCS of a circular disk.

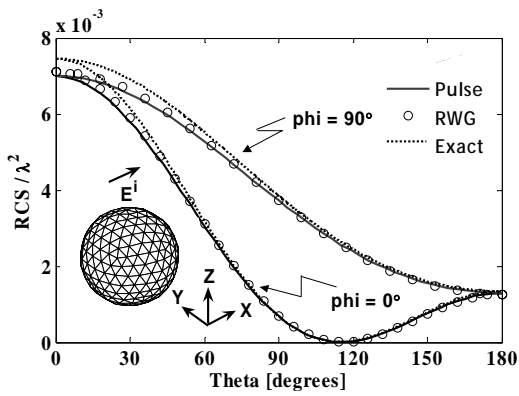


Figure 5: Bistatic RCS of a sphere.

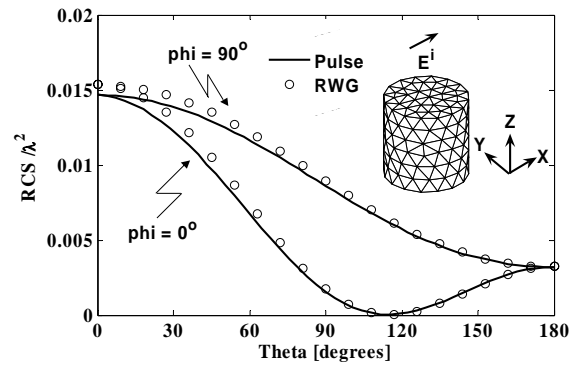


Figure 6: Bistatic RCS of a circular cylinder.

Computational Electromagnetic Field Calculation by means of Finite Integration Technique (FIT) and/or Method of Moment (MoM)

A.Ciccomancini Scogna[#], M. Strydom[#]

[#] CST of America Inc, 10 Laurel Avenue, Suite 300, Wellesley Hills (MA) 02481 USA - antonio.ciccomancini@cst.com ,
marli.strydom@cst.com

Abstract – The present paper offers an overview of two computational electromagnetic methods: Finite Integration Technique (FIT) and Method of Moments (MoM) with the enhancement of the Multilevel Fast Multipole Method (MLFMM). Both methods are the solution in the integral form of Maxwell equations, with both methods having their specific advantages. A number of examples, covering different fields of applications ranging from high speed printed circuit boards (PCBs), packages and electromagnetic bandgap structures (EBGs) to antennas and radar-cross-section (RCS) problem-types are analyzed and validated by means of measured data, other numerical techniques and/or analytical formulations. It is illustrated how FIT can be implemented with both hexahedral and tetrahedral meshes, offering in this way the possibility to study the same problem with two different approaches and validating therefore the numerically calculated results. It is finally discussed how MoM in combination with the MLFMM is well suitable for the solution of large problems ($30-50\lambda$) due to the linear scalability $O(N\log N)$ of the matrix calculation.

1. Introduction

Efficient and accurate simulations of electromagnetic fields are more important than ever in the industrial construction and design optimization of electromagnetic technical devices. Increasingly, topics such as electromagnetic compatibility (EMC), electromagnetic interference (EMI), as well as the related signal integrity (SI) and power integrity (PI) become important due to the ongoing miniaturization and higher operating frequencies of devices. In many cases, analytical approaches and/or circuit level simulations can not predict sufficiently the functionality of the electrical devices, and full wave simulations need to be used.

Stringent time-to-market requirements mean that there is no time for time consuming prototyping activities in which measurements can be carried out in proper facilities. Consequently, computation of the electromagnetic (EM) behaviour of a circuit has replaced direct measurements in the prototyping phase.

Numerical techniques generally require more computation effort than analytical techniques or expert systems, since they attempt to solve fundamental field equations directly, subject to the boundary constraints posed by the geometry. Without making a priori assumptions about which field interactions are most significant, numerical techniques analyze the entire geometry provided as input.

In the *full-wave* (field based) approach, Maxwell's full electrodynamics equations are solved without any simplification such as in the quasi-static approach. Discretization of Maxwell's equations is applied in the region of interest to find the approximate electric (E) and magnetic (H) field components at various locations in the system.

Once the approximate field components are obtained, equivalent current and voltage can be simply calculated by means of the following equations:

$$\begin{aligned} V_{ba} &= -\int_a^b \vec{E} \times dl \\ I &= \int_c \vec{H} \times dl \end{aligned} \quad (1)$$

In (1) c denotes a closed path encircling the conductor with electric current flowing within it, while a and b denote two different points on the conducting structures of the model.

Note that both the relations (1) are only accurate where quasi-static mode and quasi-transverse electric magnetic (TEM) propagation mode is valid in the system.

For very high frequency systems we usually do away with the notion of voltage and current, it is simply the interaction of the E and H fields in the system and the physics of each component that determines the outcome.

A number of different numerical techniques for solving electromagnetic problems are available and each numerical technique is usually well-suited for the analysis of a particular type of problem. In this work two numerical methods are discussed: FIT and MoM; these methods are both implemented in the commercial software CST Studio Suite 2006BTM

The paper is organized as follows: in the next section an introduction of the FIT is provided along with an overview of different applications resolved in time and/or frequency domain. Next the MoM and the MLFMM are briefly described and applications are presented as well. Finally some concluding remarks pointing out the advantages/disadvantages of both numerical methods are discussed.

2. The Finite Integration Technique (FIT)

Finite Integration Technique (FIT) was first proposed by T. Weiland [1-2]. This numerical method discretizes the integral form of Maxwell's equations and provides a universal spatial discretization scheme, applicable to various electromagnetic problems, ranging from static field calculations to high frequency applications in time or frequency domain.

$$\int_S \vec{E} \cdot \vec{n} dS = \frac{1}{\epsilon_0} \int \rho dV \quad (2)$$

$$\oint_C \vec{E} \cdot d\vec{C} = -\frac{d}{dt} \int_S \vec{B} \cdot \vec{n} dS \quad (3)$$

$$\int_S \vec{B} \cdot \vec{n} dS = 0 \quad (4)$$

$$\oint_C \vec{B} \cdot d\vec{C} = \mu_0 I + \mu_0 \epsilon_0 \int_S \frac{\partial}{\partial t} \vec{E} \cdot \vec{n} dS \quad (5)$$

In order to numerically solve Maxwell's equations a finite calculation domain is defined, enclosing the considered application problem. By creating a suitable mesh system, this domain is split up into several small cuboids, so-called grid cells. The spatial discretization of Maxwell's equations is finally performed on two orthogonal grid systems, where the new degrees of freedom are introduced as integral values as well.

Referring to Figure 1a, the electric grid voltages \mathbf{e} and magnetic facet fluxes \mathbf{b} are allocated on the primary grid G and the dielectric facet fluxes \mathbf{d} as well as the magnetic grid voltages \mathbf{h} on the dual grid \tilde{G} (indicated by the tilde).

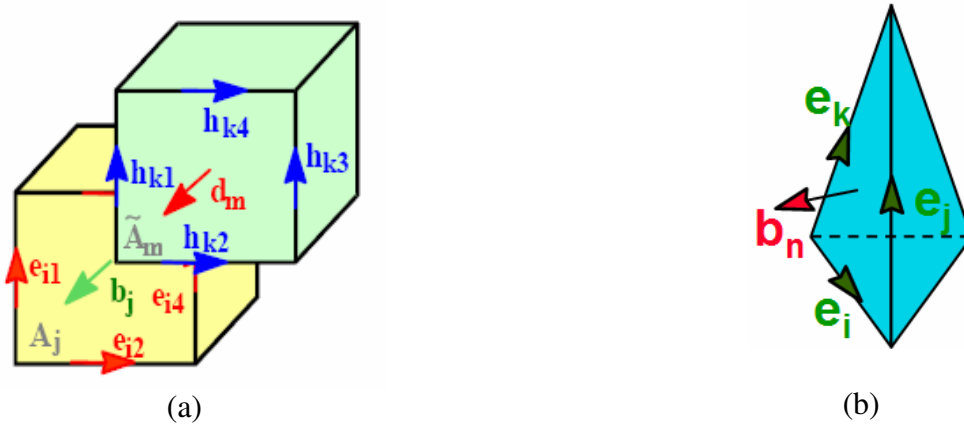


Figure1 – a): Hexahedral mesh with dual discretization grid for electric and magnetic fluxes, b): Tetrahedral mesh representation for frequency domain solver.

As an example, consider Faraday's law. The closed integral on the equation (3) can be rewritten as a sum of four grid voltages without introducing any supplementary errors (6-7). Consequently, the time derivative of the magnetic flux defined on the enclosed primary cell facet represents the right-hand side of the equation (3).

By repeating this procedure for all available cell facets, the calculation rule can be summarized in a matrix formulation, introducing the topological matrix \mathbf{C} as the discrete equivalent of the analytical curl operator (8)

$$\oint_{\partial A_n} \vec{E} \cdot d\vec{s} = -\frac{\partial}{\partial t} \iint_{A_n} \vec{B} \cdot d\vec{A} \rightarrow \mathbf{C}e = -\frac{\partial}{\partial t} \mathbf{b} \quad (6)$$

$$e_i + e_j - e_k - e_l = -\frac{\partial}{\partial t} b_n \quad (7)$$

$$\begin{pmatrix} \dots & & & \\ 1 & 1 & -1 & -1 \\ \dots & & & \end{pmatrix} \begin{pmatrix} e_i \\ e_j \\ e_k \\ e_l \end{pmatrix} = -\frac{\partial}{\partial t} \begin{pmatrix} \cdot \\ b_n \\ \cdot \end{pmatrix} \quad (8)$$

In addition to orthogonal hexahedral grids, FIT can also be applied to more general mesh types such as topologically irregular grids and tetrahedral grids, respectively. Figure 1b shows the allocation of the electric voltages and magnetic fluxes on a tetrahedral mesh cell. It is straightforward to derive the corresponding equivalent representation of (7):

$$e_i + e_j - e_k = -\frac{\partial}{\partial t} b_n \quad (9)$$

Applying this scheme to Ampere's law on the dual grid involves the definition of a corresponding discrete curl operator $\tilde{\mathbf{C}}$. Similarly the discretization of the remaining divergence equations introduces discrete divergence operators \mathbf{S} and $\tilde{\mathbf{S}}$, belonging to the primary and dual grid, respectively. As previously indicated, these discrete matrix operators just consist of elements '0', '1' and '-1', representing merely topological information. Finally we obtain the complete discretized set of the equations.

$$\mathbf{C}\hat{\mathbf{e}} = -\frac{d}{dt}\hat{\mathbf{b}} \quad (10)$$

$$\tilde{\mathbf{C}}\hat{\mathbf{h}} = \frac{d}{dt}\hat{\mathbf{d}} + \hat{\mathbf{j}} \quad (11)$$

$$\mathbf{S}\hat{\mathbf{b}} = \mathbf{0} \quad (12)$$

$$\tilde{\mathbf{S}}\hat{\mathbf{d}} = \mathbf{q} \quad (13)$$

In these equations $\hat{\mathbf{e}}$ and $\hat{\mathbf{h}}$ denote the electric fields between grid points and the magnetic fields between dual grid points, respectively.

Vectors $\hat{\mathbf{d}}$, $\hat{\mathbf{b}}$ and $\hat{\mathbf{j}}$ are fluxes over the grid or dual grid faces. In (13) \mathbf{q} represents the electric charges. Due to the consistent transformation, analytical properties of the fields are maintained resulting in corresponding discrete topological operators on the staggered grid.

It should be mentioned that no additional error has yet been introduced and this essential point of FIT discretization is reflected in the fact that important properties of the continuous gradient, curl and divergence operators are still maintained in grid space.

The spatial discretization of a numerical algorithm could cause long term instability, however, it can be shown [1] that the FIT formulation is not affected by such problems, since the set of equations

maintain energy and charge conservation. The discrete analogue of the coupling between fields and fluxes is represented by the material diagonal matrices \mathbf{M}_E , \mathbf{M}_H and \mathbf{M}_K

$$\hat{\mathbf{d}} = \mathbf{M}_E \hat{\mathbf{e}} \quad (14)$$

$$\hat{\mathbf{h}} = \mathbf{M}_H \hat{\mathbf{b}} \quad (15)$$

$$\hat{\mathbf{j}} = \mathbf{M}_K \hat{\mathbf{e}} + \hat{\mathbf{j}}_A \quad (16)$$

The absorbing boundary conditions of the calculation domain are implemented as a perfectly matched layer (PML). Whereas the classical FDTD has the disadvantage of the staircase approximation of complex boundaries, the Perfect Boundary Approximation (PBA) [3], Thin Sheet Technique (TST), and the Multilevel Subgridding Scheme (MSS), applied in conjunction with FIT maintain all the advantages of the structured Cartesian grids, i.e. high memory efficiency and simulation speed, while allowing an accurate modeling of curved boundaries and fine details with a provable better convergence than the staircase approximation.¹ The discretization of the time derivative is formulated as an explicit algorithm, in leap-frog form. For the lossless case, the integration scheme is described by the following two equations and graphically illustrated in Figure 2.

$$\hat{\mathbf{h}}^{(m+1)} = \hat{\mathbf{h}}^{(m)} - \Delta t \mathbf{M}_H \mathbf{C} \hat{\mathbf{e}}^{(m+1/2)} \quad (17)$$

$$\hat{\mathbf{e}}^{(m+3/2)} = \hat{\mathbf{e}}^{(m+1/2)} + \Delta t \mathbf{M}_E^{-1} \left(\tilde{\mathbf{C}} \hat{\mathbf{h}}^{(m+1)} - \hat{\mathbf{j}}^{(m+1)} \right) \quad (18)$$

The marching-on-time requires in this case only one matrix-vector multiplication, therefore reducing the computational resources ((10) – (13)).

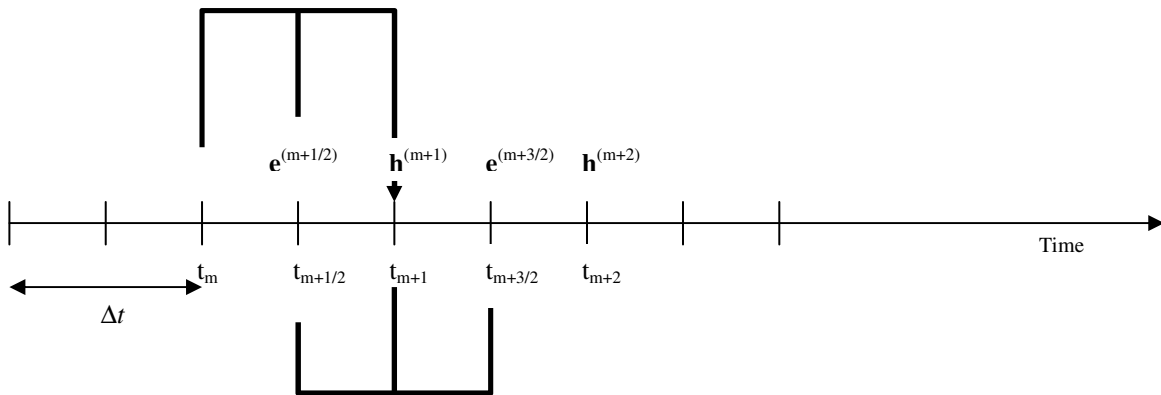


Figure 2 - The leap-frog scheme

¹ CST STUDIO SUITE 2006B™, Perfect Boundary Approximation (PBA) ©, Thin Sheet Technique (TST)™ and Multilevel Subgridding Scheme (MSS)™ are trademarks or registered trademarks of CST GmbH, Germany.

This time stepping scheme coincides with the well-known FDTD-algorithm by Yee [4], which was originally derived for uniform Cartesian grids with discrete electric and magnetic field intensities instead of fluxes and voltages.

Since the FDTD scheme is an explicit time marching scheme, it has to full fill the Courant-Friedrich-Levi (CFL) criterion for a maximum stable time step length:

$$\Delta t < \frac{1}{c \sqrt{\frac{1}{\Delta x^2} + \frac{1}{\Delta y^2} + \frac{1}{\Delta z^2}}} \quad (19)$$

which is here given for a three-dimensional Cartesian grid taking into account a possible non-homogeneous material distribution within a cell complex with non-uniform grid spacing.

To briefly summarize, FIT (in time domain) is a discretization method which transforms Maxwell's equations onto a dual grid cell complex, resulting in a set of discrete matrix equations. The degrees of freedom collected in the vectors of this discretization scheme, typically consist in physically measurable, integral quantities such as voltages, currents or charges.

This discretization approach results in sparse integer matrices, \mathbf{C} , $\tilde{\mathbf{C}}$, \mathbf{S} and $\tilde{\mathbf{S}}$ which only contains information on the incidence relations of the dual cell complex. This mere restriction to topological information of the grid is responsible for the typical complex property $\mathbf{S}\mathbf{C} = \mathbf{0}$ and $\tilde{\mathbf{S}}\tilde{\mathbf{C}} = \mathbf{0}$. In connection with the relation $\mathbf{C} = \tilde{\mathbf{C}}^T$ due to duality of the grid pair and with symmetric and positive definite material matrices \mathbf{D}_ϵ and \mathbf{D}_μ the relations of these incidence matrices allow to prove energy and charge conservation of the spatially discretized equations.

3. FIT applications

3.1 Photonic bandgap structure

Photonic bandgap (PBG) structures [5] are periodic structure in which propagation of certain bands of frequencies is prohibited. Original PBG research was done in the optical region, but PBG properties are scalable and applicable to a wide range of frequencies.

In the last few years there has been an increasing interest in microwave and millimeter-wave application PBG structures. PBG can be achieved by using metallic, dielectric, ferromagnetic or ferroelectric implants.

Figure 3 illustrates a typical PBG structure realized with a two dimensional (2D) square lattice with circles etched in the ground plane.

A 50 ohm mender line runs over the etched ground plane from one side to the substrate to the other and scattering parameters (S-parameters) are calculated by means of FIT and compared with measured results (see Figure 4). The frequency range is 0-6GHz and a good agreement can be observed for both S_{11} and S_{21} magnitude.

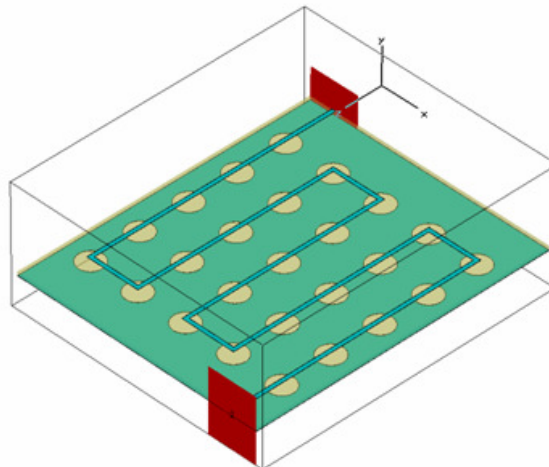


Figure 3 - PBG structure

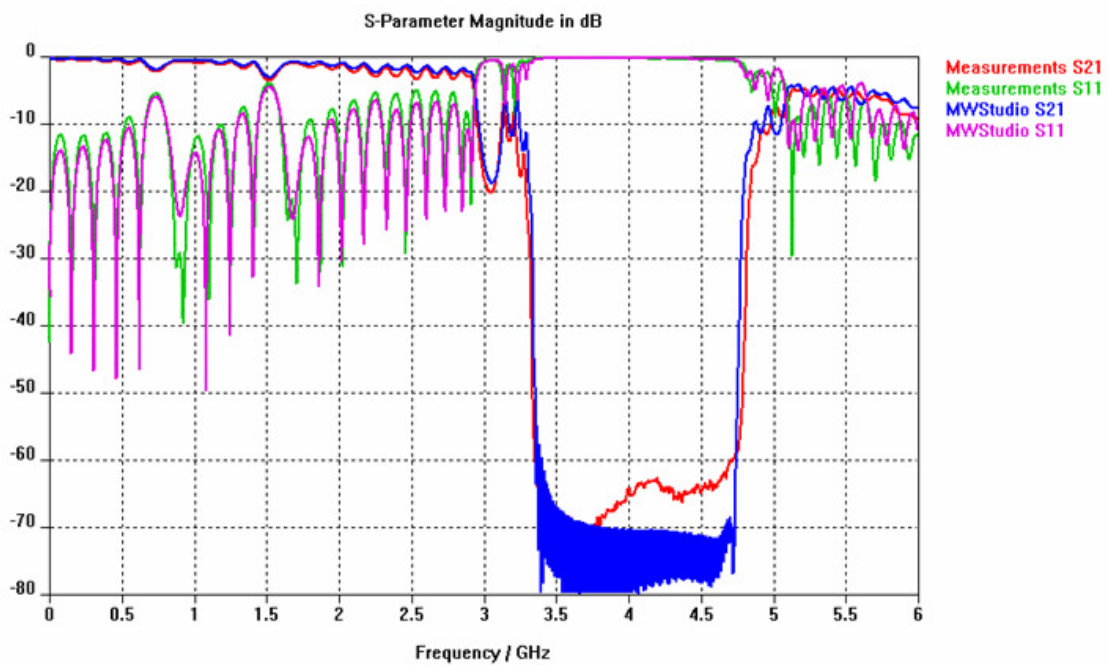


Figure 4 - S-parameters results (S_{11} , S_{12}): comparison between measured and simulated FIT (MWStudio) results.

3.2 Design of EBG structures

Simultaneous switching noise (SSN) or ground bounce noise (GBN) is one of the major concerns for the high-speed digital computer systems with fast edge rates, high clock frequencies, and low voltage levels.

The resonance modes between the power and ground (PWR/GND) planes excited by the SSN causes significant SI problems and EMI issues for the high-speed circuits, therefore the elimination of this noise is essential.

Adding decoupling capacitors to create a low impedance path between PWR/GND planes is a typical way to suppress SSN. However, in general, these capacitors are not effective at frequencies higher than 600 MHz due to their finite lead inductance.

The embedded capacitance with a very thin dielectric is another possible solution to suppress SSN; nevertheless the electromagnetic waves still propagate between the planes with resonance at specific frequencies. A hybrid method which is considered to be an alternative to the use of decoupling capacitors is represented by virtual island (or gapped planes) and shorting vias.

The shorting vias are used to provide the return current path with low impedance and the virtual islands are used to block the PPW noise propagation through PWR/GND plane pairs; even with this methodology the noise suppression is only possible for very narrow band frequency ranges.

Recently, a new idea for eliminating the SSN is proposed by designing EBG structures [6-8]. When inserting an EBG structure in the parallel-plate waveguide-like structure of the Power Distribution Network (PDN) of a Printed Circuit Board (PCB), a resonant circuit composed of the top plate, a single patch, the corresponding via and the plane that connects the vias together is created.

This circuit provides a low-impedance path to high-frequency currents in the PWR planes suppressing propagation within specific frequency ranges.

There are a few primary closed form formulas for describing properties of EBG periodic structures using lumped elements model when the structure is small enough compared to wavelength: the parallel LC resonator which acts like a band stop filter is one of them.

Other models are also available in literature, but to the best of our knowledge there is no exact or even reasonably accurate closed formula that relates the geometrical parameters of the EBGs to the frequency of band stop.

Therefore, and until a highly accurate closed form expression is developed, the effective band of an EBG structure needs to be generated directly or indirectly using numerical simulation tools.

When using numerical codes to extract the effective band of these structures, several techniques are available, but two methods are commonly used: 1) direct method and 2) indirect method.

In the first one the S-parameter between two ports placed across the EBG structures (S_{21}) is evaluated, while in the second one the so-called dispersion diagram is calculated.

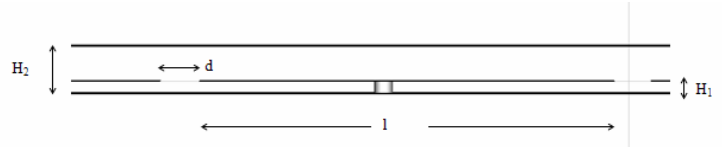
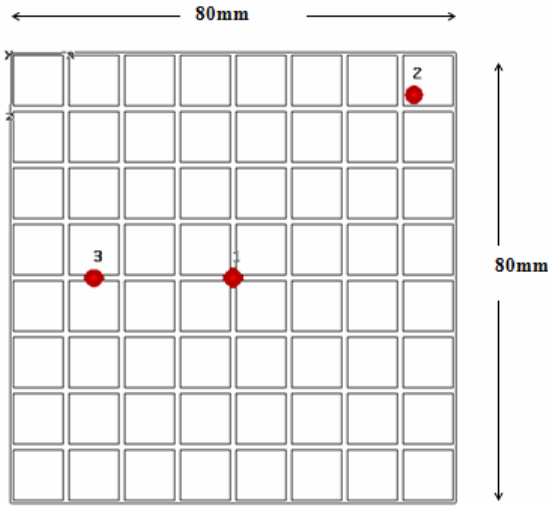
Such diagram describes the propagation characteristics of an infinitely periodic structure composed of EBG patches.

3.2.1 Direct method

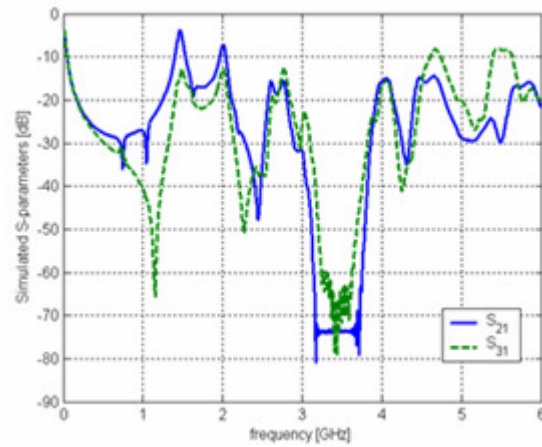
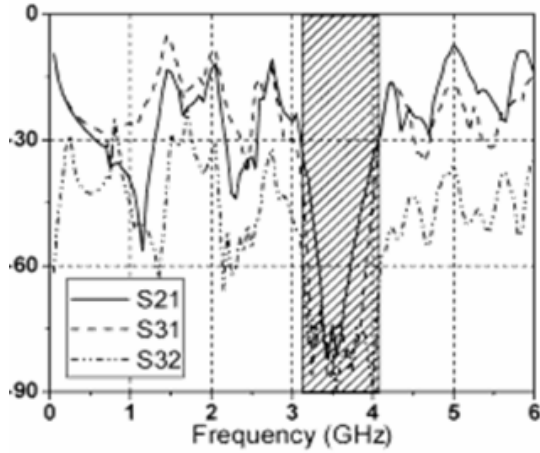
Figure 5 represents the top view and the stack up of a standard PCB with EBG structure consisting on squared patches.

The outline of entire structure is 80 by 80 mm and the EBG patch layer has 8x8 square patches. The other parameters are: $H_1=0.25$ mm, $H_2=1$ mm, $d=1$ mm and $l=9$ mm.

The behavior of the structure is probed at three ports: Port 1, Port 2, and Port 3, as illustrated in the figure. For comparison, a solid plane pair with the same dimensions but without the EBG patch layer is studied as well. The simulated and measured transmission coefficients are shown in the same figure. The band gap region is well defined in both simulation and measured data and a good agreement is observed over the all frequency range.



(a)



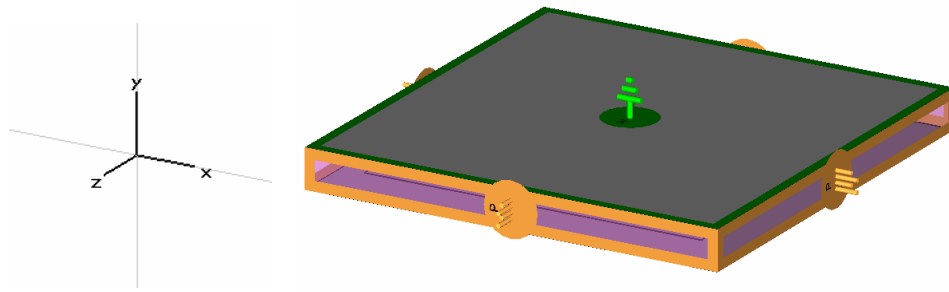
(b)

Figure 5 a): EBG model, top view and cross section, b): S-parameters results (S_{21} , S_{31}): comparison between measured and simulated FIT results.

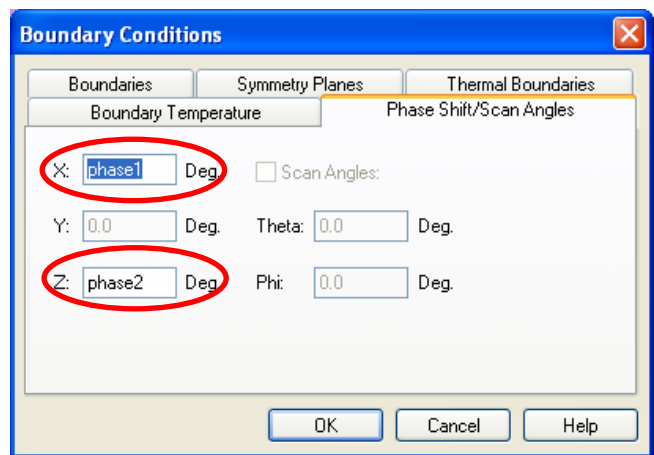
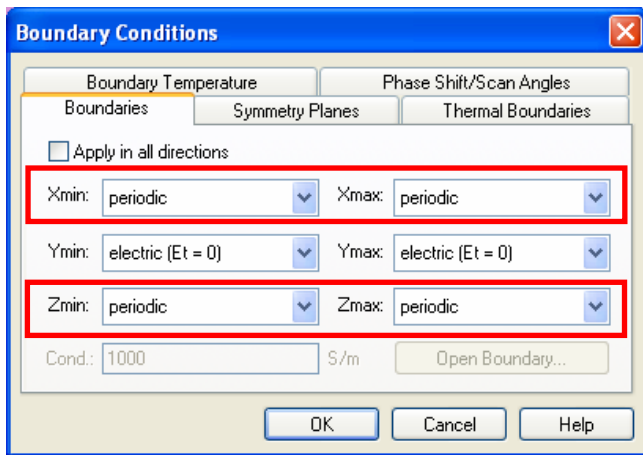
3.2.2 Indirect method

The indirect method consists on the evaluation of dispersion diagrams which represent propagating modes and band gaps that can potentially exist between such modes. This kind of analysis can be performed by means of eigenmode solver and periodic boundary conditions with phase shift (scan angle) parameterized.

Figure 6 illustrates a typical unit cell and the settings used for the boundary conditions in the full wave simulation. The results are reported in Figure 7, which illustrates the dispersion diagram (with in evidence the band gaps between modes) for the structure presented in Figure 5.



(a)



(b)

Figure 6 – a): Unit cell mode and b): periodic boundary conditions definition

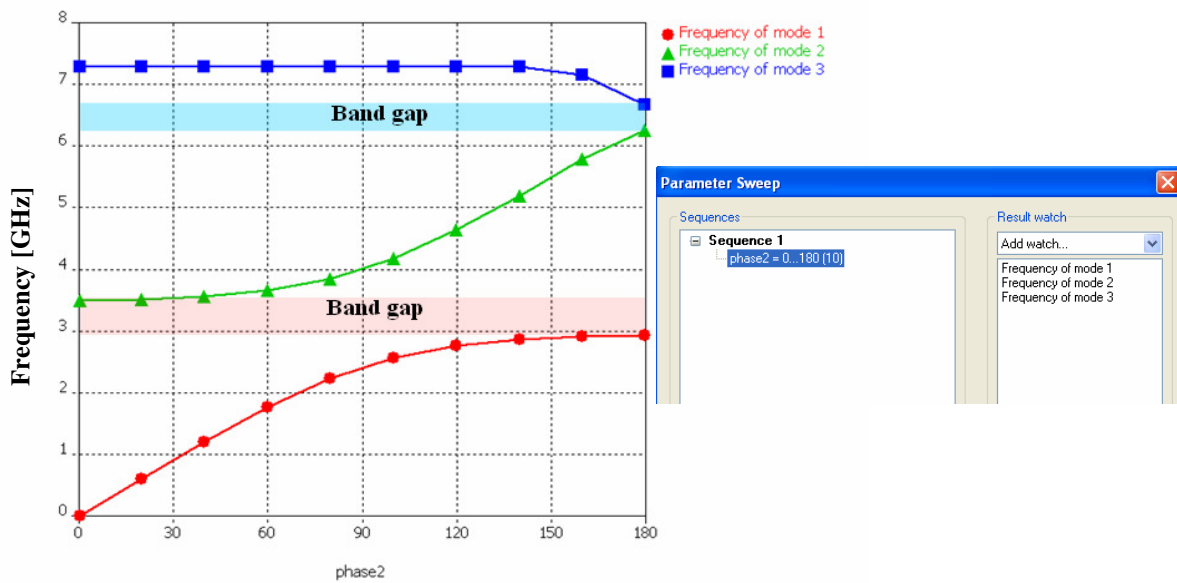
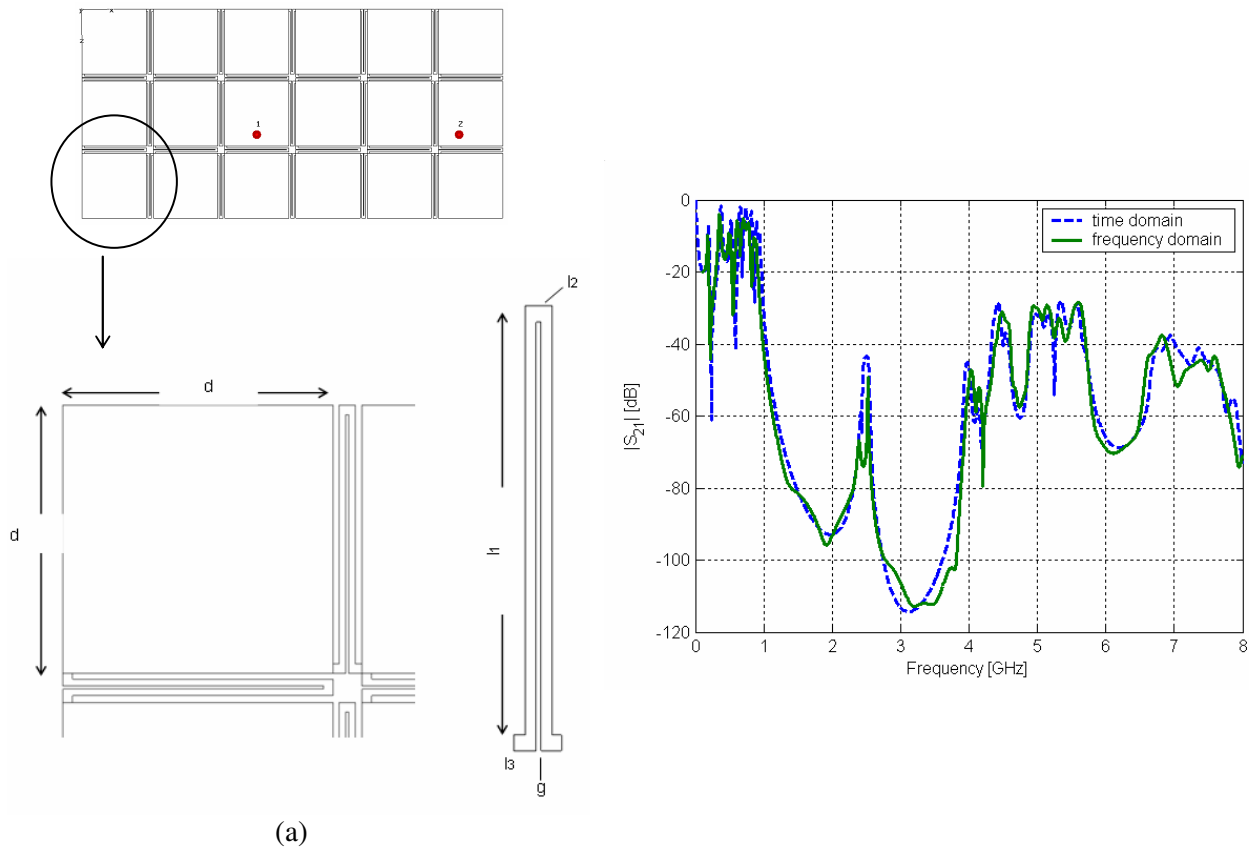


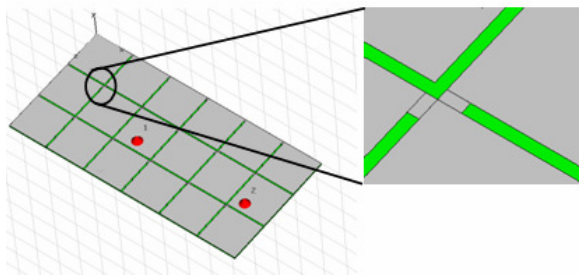
Figure 7 - Dispersion diagram.

One of the main concerns of using EBG structures for SSN noise suppression is related to their cost, which can be very high. For this reason during the last few years 2D EBG structures have been proposed and extensively used for ultra wide band (UWB) noise mitigation and mixed-signal systems. For example Figure 8a represents a test board used to analyze the performance of the two different EBG structures, it is a 9.15x4.15cm board with FR4 dielectric ($\epsilon_r=4.4$ and $\text{tang}\delta=0.02$ at 0.5GHz). The EBG layer [11] is characterized by square patches with edge $d=1.4\text{mm}$ and double L branches; the parameters are listed in TABLE II. The S-parameters are reported in the same figure, where a direct comparison between time and frequency domain FIT solver is provided. Figure 8b represents another possible design of the metal patches [9-10] for the same test board and it consists in two connected simple metal branches.



parameters	d	l₁	l₂	l₃	g
[cm]	1.4	1.35	0.085	0.095	0.055

TABLE II – EBG CELL DIMENSIONS



(b)

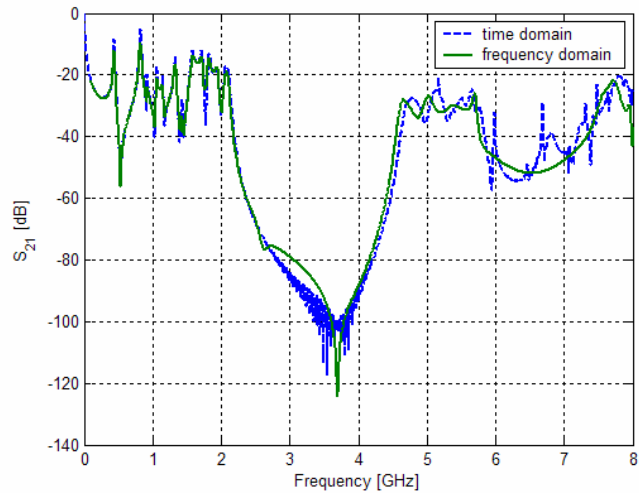
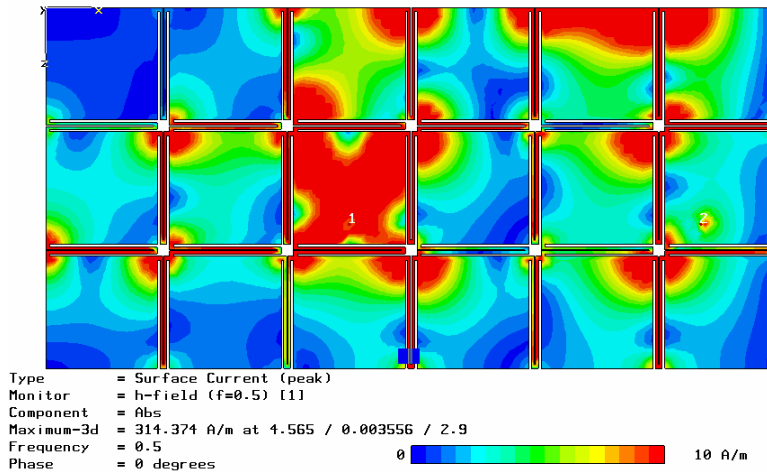


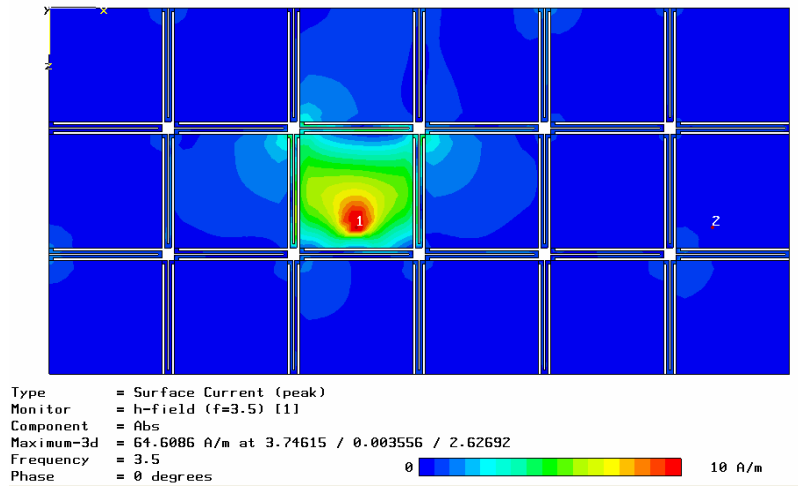
Figure 8 – 2D alternative EBG structures, S_{21} : comparison between time domain (TD) and frequency domain (FD).

Figure 9 illustrates the surface current distribution at different frequencies for the board with continuous PWR plane and the board with EBG structure (Figure 8a).

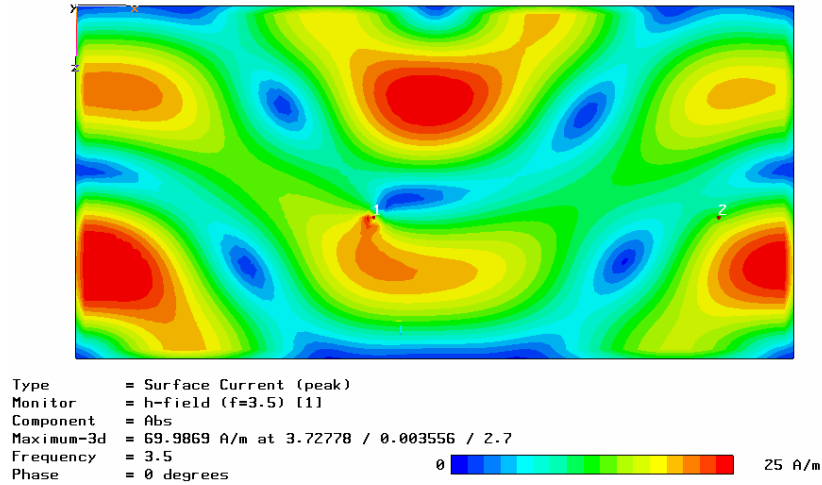
The current variation is represented by a color contrast in these figures and the unit in the color bars is in [A]. Isolation is of course desirable between the two ports 2 in this example. Figure 9a shows that the EBG structure does not provide good isolation at 500 MHz since this frequency is still in the pass band region. Figure 9b shows the current distribution on the EBG structure at 3.5 GHz, which is a frequency value in the stop band region. The noise generated by the current source on the input port can not propagate to the other metal patches characterizing the EBG structure which means that eventual noise generated by digital circuits can not propagate to the RF circuits located at the output port 2. It should be also noted that the scale for the surface current distribution in Figure 9a, b is reduced to 0-10 [A/m] in order to better visualize the surface current pattern around the input port.



(a)



(b)



(c)

Figure 9 - Surface current distribution at (a): 0.5GHz on EBG plane, (b): 3.5GHz on EBG plane and (b) 3.5GHz on continuous reference plane

3.3 Stripline and SMA connectors in multilayer stack up structure

At bitrates above one Gb/s the effects of boards' discontinuities on the integrity of the signals can not be neglected. For a correct design, the effects of parasitic, packaging, boards' materials and traces' geometries must be characterized and quantified. An essential step in this process of characterization is the measurement of the properties of the board in terms of S-parameters, input impedance, noise voltage, etc. [12]. Microstrip and stripline structures can not be connected directly to the coaxial ports of a network analyzer (NA).

The structure or device under test must be physically connected to the NA by some kind of transition network or fixture. One of the most frequently used fixture or connector for this kind of applications is the surface mounted adapter (SMA) [13-14].

From engineering point of view the interesting properties of an SMA connector, and hence, the equivalent circuit able to predict those properties, are those of an SMA mounted on a board and not simply isolated.

Because of this it has been chosen to characterize two SMA connected to a stripline (1859mils long), according to the multi-layers stack-up illustrated in Figure 10.

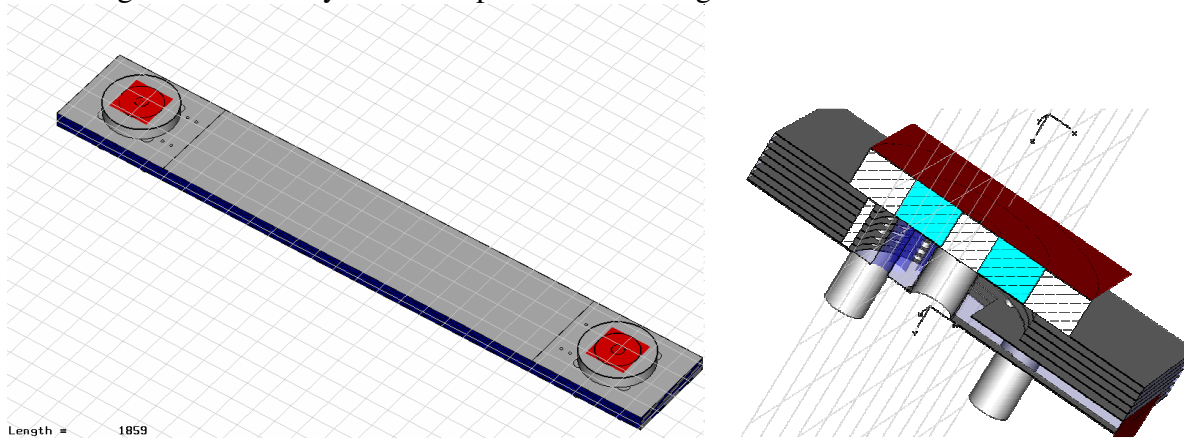


Figure 10 – 3D view of the simulated structure and SMA connector

Figure 11 illustrates the results due to the 3D FIT simulation and the comparison with the measured results: the frequency range is from few MHz up to 20GHz and how it is possible to see a good accuracy is achieved.

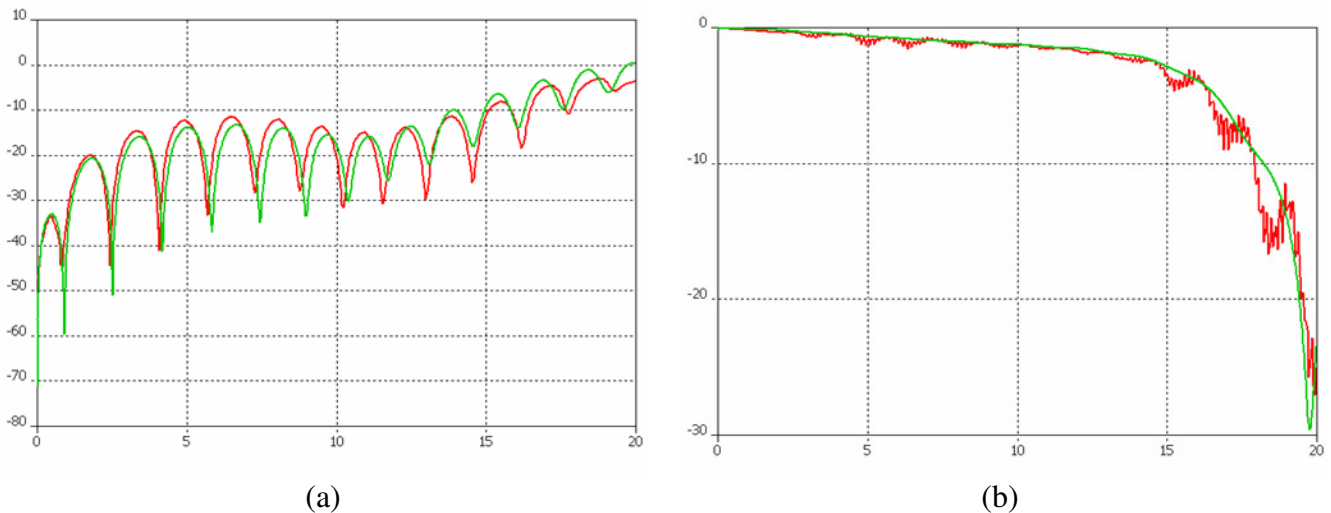


Figure 11 – Comparison between simulated and measured results, a): $|S_{11}|$, b): $|S_{12}|$

3.4 Advanced Modeling and Measurement of Wideband Horn Antennas

Dual-ridge horn antennas are commonly used as wideband gain standards for antenna measurements. The horn is characterized by connectors and essentially is open with only flared ridge waveguide with lateral bars. It is designed to harmonize the gain with the frequency curve.

At low frequencies the bars appear as a closed surface and increase the bore sight gain of the horn, whereas at high frequencies the bars are electrically transparent and the effective gain decreases.

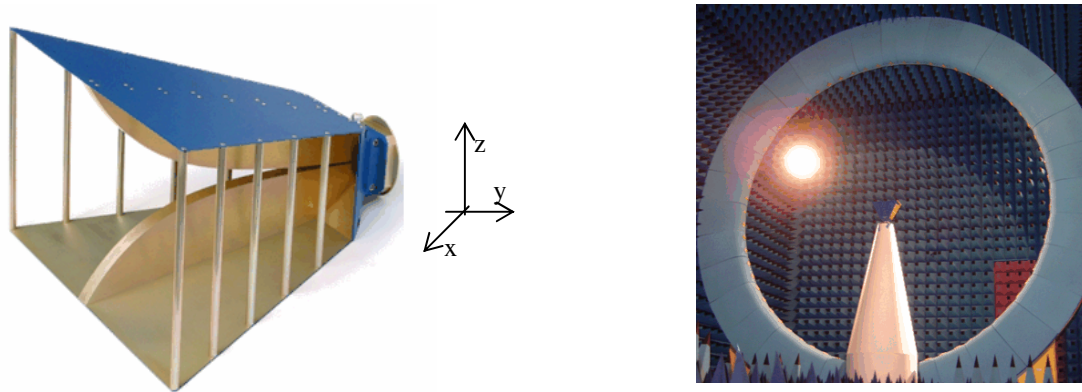


Figure 12 – 3D view of the simulated horn antenna and anechoic chamber used to perform measurements.

The antenna is modeled and simulated with the FIT code by using magnetic symmetry condition in the xz-plane of the antenna and a rather coarse regular mesh with $\lambda/10$ spacing.

The used connectors are approximated with simple structures, and dielectric materials are ignored. For the calculations, PEC is assumed for the metallic parts, and PML (Perfect Matching Layer) absorbing boundary conditions are used. The required CPU time for a full analysis is approximately four hours on a Pentium 4, 3 GHz PC.

The dual ridge horn was measured in the Satimo Stargate facility in Atlanta, USA over a frequency range of 800 MHz to 6 GHz. The simulated and measured antenna return loss performance for both amplitude and phase components at the antenna reference port is in good agreement as shown in Figure 13

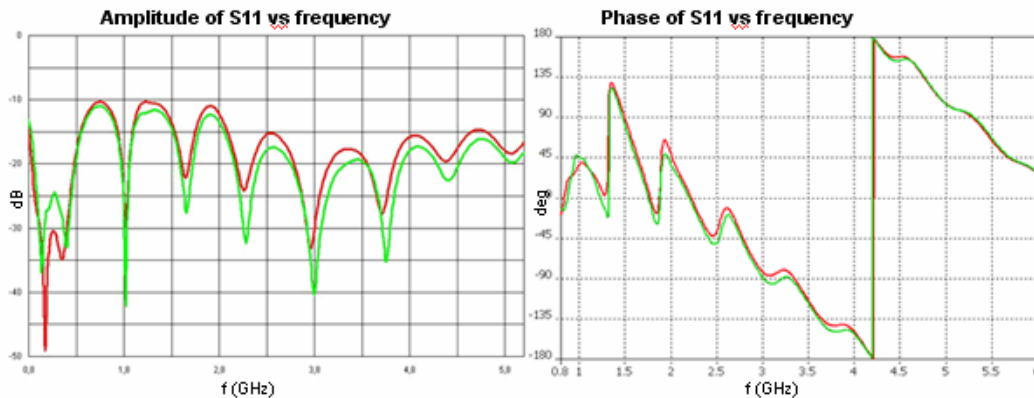


Figure 13 - Simulated with FIT and measured return loss as a function of frequency.

The results of simulated and measured bore sight directivity are plotted in Figure 14. Even in this case as excellent correlation between the two curves can be observed, and the differences fall within the measurement accuracy of the measurement equipment.

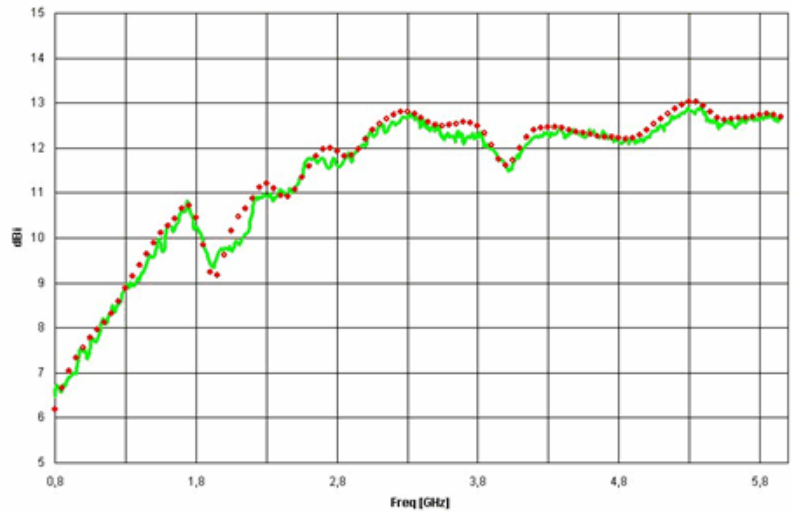


Figure 14 - Simulated with FIT and measured bore sight directivity.

Figure 15 instead shows the comparison of simulated and measured E and H plane radiation patterns at 3.6 GHz. The polarization definition is Ludwig III and it can be seen that the two curves are very close to each other.

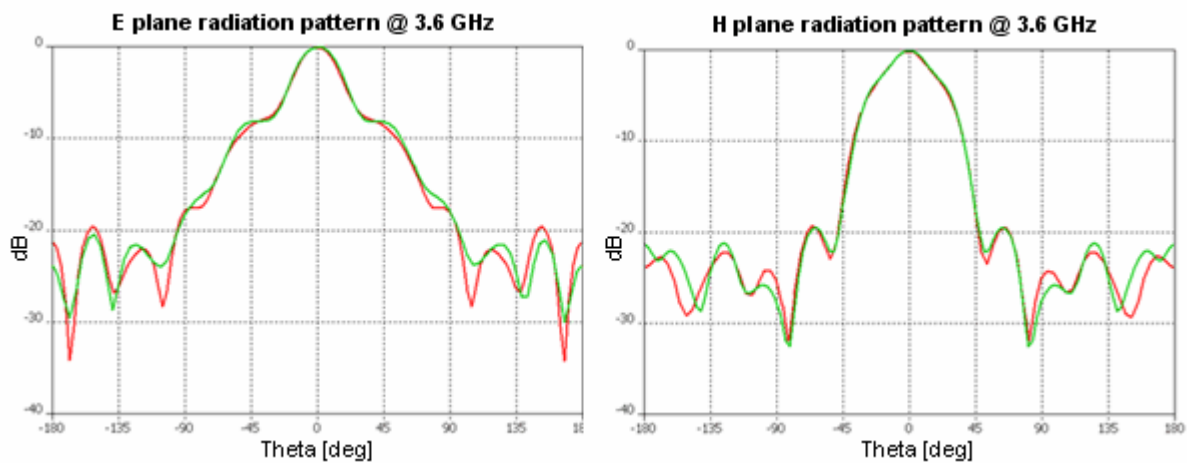


Figure 15 - Simulated and measured E and H plane patterns at 3.6 GHz

The antenna's back radiated fields are often very difficult to determine with high accuracy due to coupling between the antenna under test and the antenna positioner.

The SATIMO Stargate spherical near field system uses a Styrofoam positioner specifically designed for minimum interference with the antenna under test.

The good agreement between the predicted and measured results for the radiated back lobe of the antenna confirms the measurement accuracy in this difficult region.

4. Method of Moment (MoM) and MLFMM enhancement

The method of moments is perhaps the most well known of all computational methods due to its rich history and its widespread application in the analysis of antennas and scatterers. This technique, which was popularized by Harrington in 1967, solves complex integral equations by reducing them to a system of linear equations [15].

The equation solved by the moment method is derived from Maxwell's equations by considering the problem of a field scattered by a perfect conductor (or lossy dielectric).

This equation solved by the MoM is either the magnetic field integral equation (MFIE) or the electric field integral equation (EFIE). The derivation of these starts from the differential form of the time independent Maxwell's equations, where, for linear field qualities:

$$\begin{aligned}\nabla \times \vec{H} &= \vec{J} + i\omega\epsilon\vec{E} \\ \nabla \times \vec{E} &= -i\omega\mu\vec{H} \\ \nabla \cdot \vec{E} &= \rho / \epsilon \\ \nabla \cdot \vec{H} &= 0\end{aligned}\tag{M.1}$$

and \vec{H} , \vec{E} and \vec{J} are vector phasors.

If a volume density of charge and a volume density of current are specified by the continuity condition

$$\nabla \cdot \vec{J} = -\frac{\partial \rho}{\partial t}\tag{M.2}$$

it can be shown that there exists a pair of potential functions (\vec{A} , Φ), which satisfy a certain differential pair (shown in [16]) and which gives the electromagnetic field:

$$\begin{aligned}\vec{B} &= \nabla \times \vec{A} \\ \vec{E} &= -\nabla\Phi - \frac{\partial \vec{A}}{\partial t}\end{aligned}\tag{M.3}$$

Furthermore, by using the gauge transformation, the inhomogeneous Helmholtz equations are derived through substitution of the potential functions into Maxwell's equations; these now equate the volume current to the potential functions.

$$\begin{aligned}(\Delta + \gamma^2)\vec{A} &= -\mu\vec{J} \\ (\Delta + \gamma^2)\Phi &= -\rho / \epsilon\end{aligned}\tag{M.4}$$

where $\gamma = \omega^2 \epsilon \mu$ and they satisfy the Lorentz condition

$$\nabla \cdot \vec{A} + \frac{1}{c^2} \frac{\partial \Phi}{\partial t} = 0 \quad (\text{M.5})$$

For the method of moment formulation, the potential functions can be written as [17-18]:

$$\begin{aligned} \vec{A}(\vec{r}) &= \mu \int_V \vec{J}(\vec{r}') g(\vec{r}, \vec{r}') dV' \\ \Phi(\vec{r}) &= \epsilon \int_V \rho(\vec{r}') g(\vec{r}, \vec{r}') dV' \end{aligned} \quad (\text{M.6})$$

Where $g(\vec{r}, \vec{r}')$ is the scalar free-space Green's function given by: $\frac{e^{-jk_0|\vec{r}-\vec{r}'|}}{4\pi|\vec{r}-\vec{r}'|}$. By using the potential functions defined in (M.3), the electromagnetic fields due to surface currents on a sheet can be obtained as

$$\begin{aligned} \vec{H}(\vec{r}) &= -\int_S \vec{J}_s(\vec{r}') \times \nabla g(\vec{r}, \vec{r}') dS' \\ \vec{E}(\vec{r}) &= -i\omega\mu \int_S [g(\vec{r}, \vec{r}') \vec{J}_s(\vec{r}') + \gamma^{-2} \nabla g(\vec{r}, \vec{r}') \nabla' \cdot \vec{J}_s(\vec{r}')] dS' \end{aligned} \quad (\text{M.7})$$

where \vec{J}_s is the sum of the surface currents on both sides of the sheet and ∇' indicates that the differentiation occurs in the source coordinates.

In many practical applications however, the electric and magnetic fields are known and the current distribution is unknown. Since Maxwell's equations are linear, the fields in (M.7) can be decomposed according to the incident/scattered field formulation:

$$\begin{aligned} \vec{H}_{total} &= \vec{H}_{inc} + \vec{H}_{scat} \\ \vec{E}_{total} &= \vec{E}_{inc} + \vec{E}_{scat} \end{aligned}$$

where the incident field is the field that would exist if the scatterer were absent. It can be shown that the electromagnetic field, which is incident on a scatterer, is given by the Stratton-Chu formula [19], and by imposing the appropriate boundary condition, the EFIE and IFIE can be derived. The interested reader is referred to [19], where the derivation is shown.

For the sake of brevity, these equations will not be shown here; however, they relate the unknown surface currents to the known incident fields, making it appropriate for implementation into the MoM.

The first and one of the most crucial steps in the method of moments is to expand \vec{J}_s as a finite sum of

basis functions, such that $\vec{J}_s = \sum_{i=1}^M J_i \vec{b}_i$, where \vec{b}_i is the i^{th} basis function and J_i is an unknown coefficient.

A large variety of basis functions exist and it is beyond the scope of this introduction to discuss these. It can be shown that by defining appropriate linearly independent weighting functions, the first equation in (M.7) can be written in matrix form as [20]:

$$[\vec{H}] = [Z][\vec{J}] \quad (\text{M.8})$$

where

$$\begin{aligned} Z_{ij} &= \langle w_j, f_m(b_i) \rangle \\ \vec{J}_i &= J_i \\ \vec{H}_j &= \langle w_j, \vec{H}_{inc} \rangle \end{aligned} \quad (\text{M.9})$$

In (M.9), w_j are linearly independent weighting functions and $j=1,2,\dots,M$. M is the number of independent equations that need to be solved and $f_m(b_i)$ is the set of basis functions. In (M.8), \vec{H} contains known incident field quantities, and Z is determined by the geometry, leaving the unknown coefficients of the induced currents J_i as the values to be solved.

The specific implementation of the Method of Moments depends upon the selection of the integral field equation and the selection of the appropriate basis functions.

In the formulation above, the magnetic field integral equation (MFIE) formulation was described, but the (electric field integral equation) EFIE could also have been used.

The fast multipole method (FMM) rests on two identities, which are described in [21] and results in an analytical approximation of the Green's function:

$$\frac{e^{-jk_0|\vec{r}+\vec{d}|}}{|\vec{r}+\vec{d}|} = -\frac{jk_0}{4\pi} \oint_s e^{-j\vec{k}\cdot\vec{d}} T_L(\hat{k}\cdot\hat{r}) d^2\hat{k} \quad (\text{M10})$$

with

$$T_L(\hat{k}\cdot\hat{r}) = \sum_{l=0}^L (-j)^l (2l+1) h_l^{(2)}(k_0 r) P_l(\hat{k}\cdot\hat{r}) \quad (\text{M11})$$

There are three aspects to the FMM formulation that are important: firstly, in (M11), $k_0 r$ is pre-computed for various distances and angles and this formulation allows a truncated multipole expansion of the Greens function.

The second aspect of importance is that in FMM the interaction matrix is divided into near and far parts. Near interactions are computed as usual with the MoM and far interactions are evaluated approximately using the formulation in equation (M11). For a more detailed description of exactly how this evaluation is achieved, the reader is referred to [21].

A graphical representation of the steps is shown in Figure 16. In part (a), the standard MoM is applied to the near field interactions. Part (b) shows how the FMM defines near field and far field regions (or groups) and in part (c) a recursive hierarchy of groups is introduced. This is known as the MLFMM.

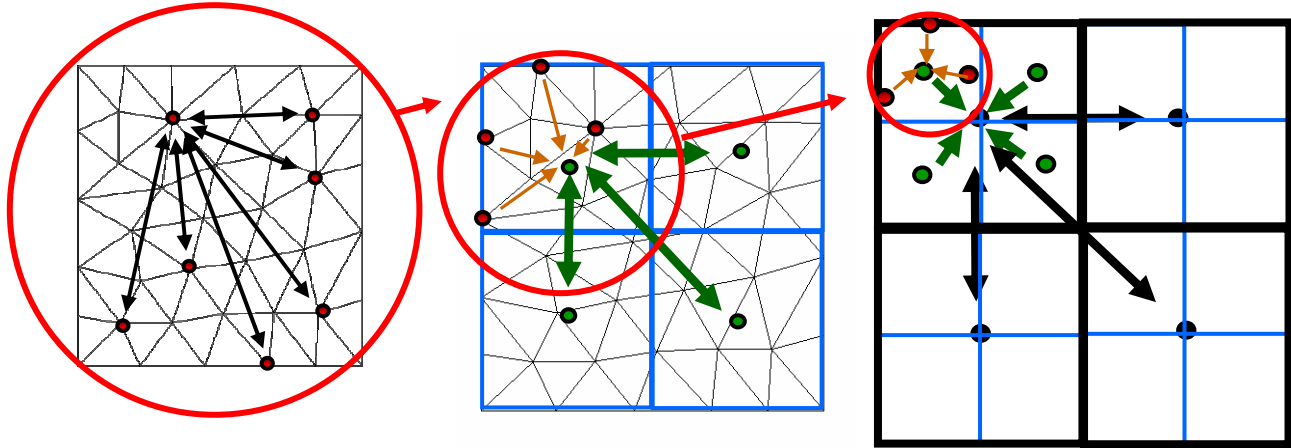


Figure 16 – MLFMM scheme representation.

It is evident from this figure that the MLFMM is very well suited for electrically large structures and for farfield or RCS applications. The MLFMM offers optimal usage of memory and minimal simulation time, while allowing models to be simulated that were previously too large to be analyzed by other numerical methods.

5. MoM applications

In the following sections few examples where the Integral solver, based on the MoM method is used, are illustrated: 1) dielectric sphere and RCS calculation, 2) almond NASA, 3) Apache helicopter.

5.1 Dielectric sphere and RCS calculation

Figure 17 illustrates 1m radius dielectric sphere ($\epsilon=1.1$, $\mu=1$) excited by means of a plane wave with $\varphi=60$, $\theta=60$ degrees. The Integral solver is used to evaluate the RCS at 100MHz on a plane at $\theta=90$ degrees and the numerical results are compared to the analytical solution, according to [22]: a good agreement is observed

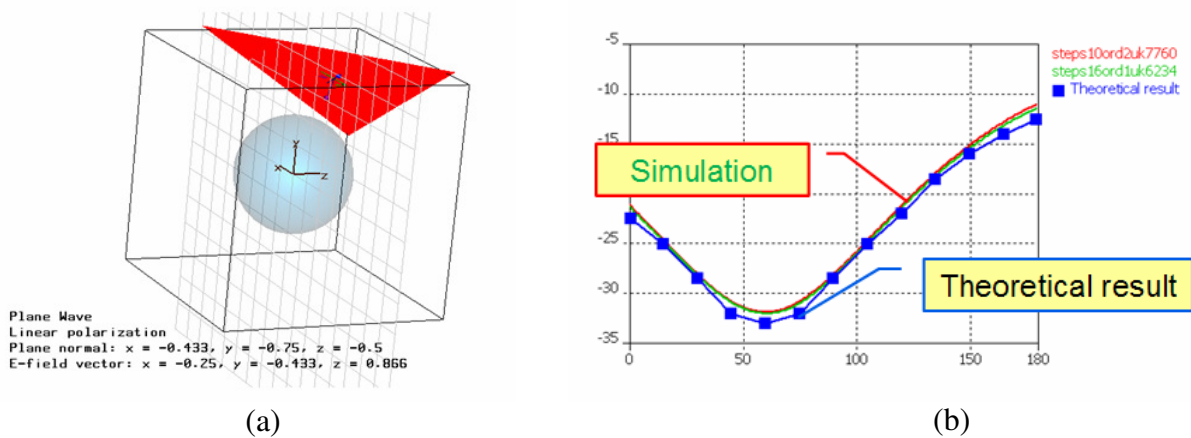


Figure 17 – a): Dielectric sphere and b): RCS results (dBm) at 100mHz

5.2 Almond NASA

The geometry of the Almond [23] is illustrated in Figure 18: a vertical plane wave excitation is applied and the angle of incidence of the polarized wave is parameterized from 0 to 180 degrees. The Almond is approximately 9.936 inches long and is defined as a PEC, more details can be found in [23]. RCS results at three distinctive frequencies, surface current distribution and Electric field are illustrated respectively in Figure 19 and Figure 20.

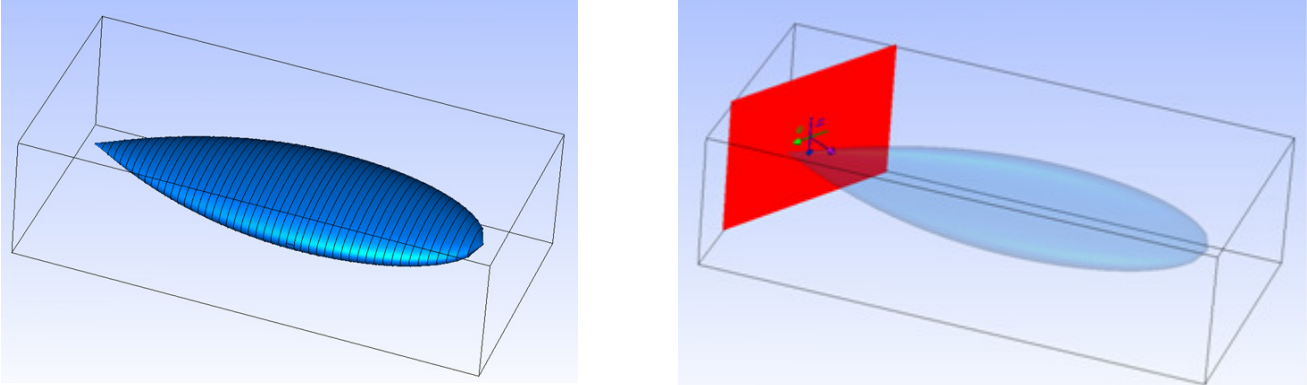
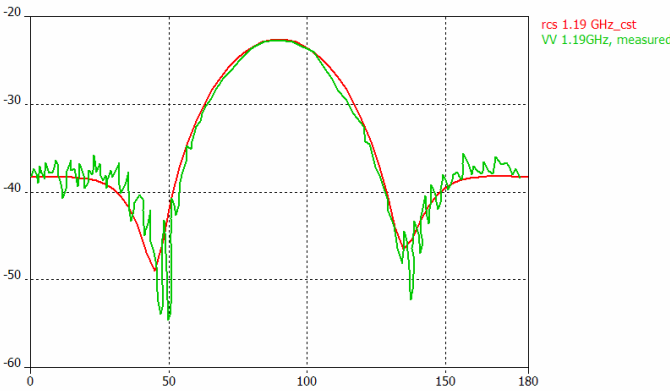
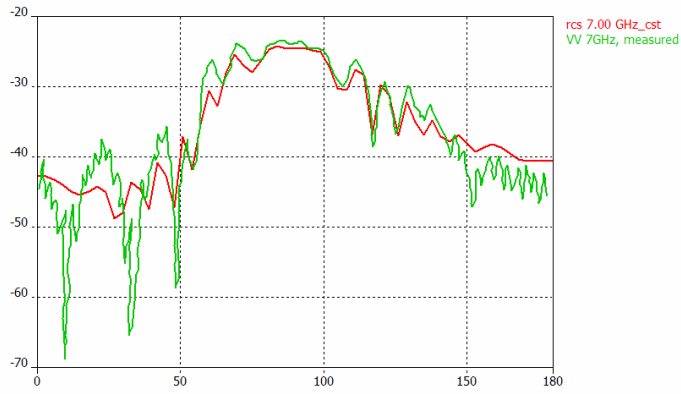


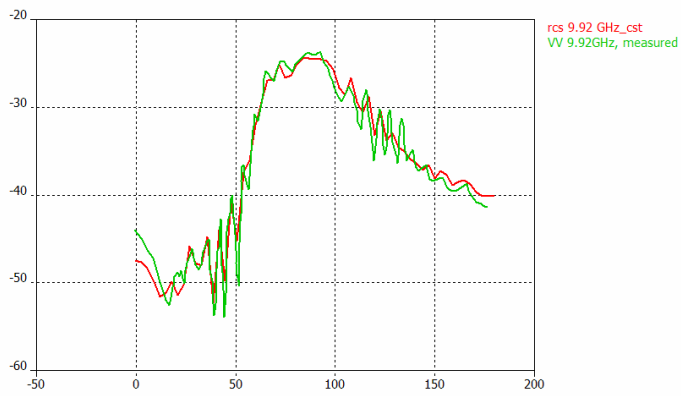
Figure 18– 3D view of the almond NASA and plane wave excitation



(a)



(b)



(c)

Figure 19– RCS calculation: comparison between measured and simulated MoM results, a) 1.19GHz b): 7GHz and c): 9.92GHz.

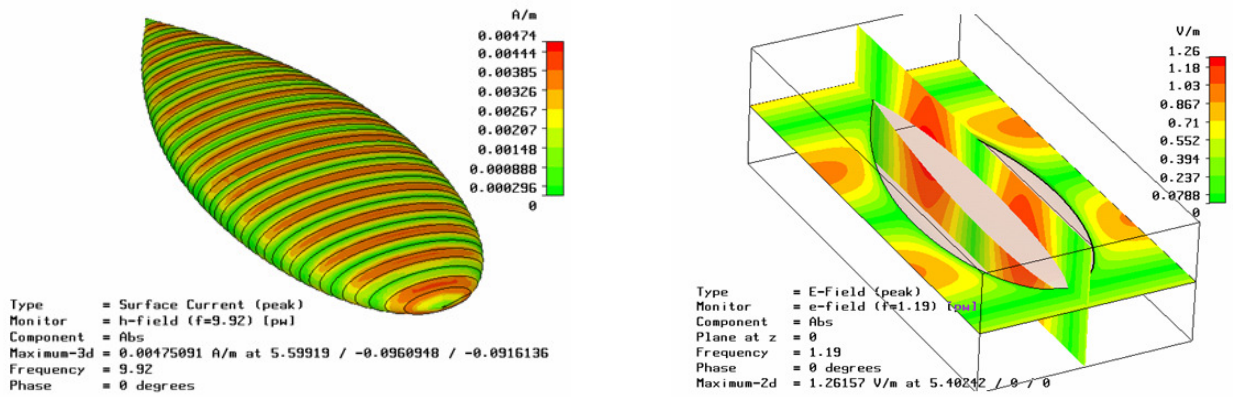


Figure 20 – Surface current distribution and Electric field on two intersecting planes

5.3 RCS and Surface Current calculation for an Apache Helicopter

This example demonstrates the simulation of an electrically large helicopter. The length of the helicopter is about 7.8 meters and, therefore, the aircraft is approximately 180 wavelengths in size. The helicopter is illuminated by a plane wave at 7 GHz and the surface mesh is represented by about 830.000 surface cells. Accordingly, the simulation is performed using more than 1.25 million unknowns.

Figure 21 shows the plane wave illumination of the helicopter at 7 GHz: the electric field vector for the plane wave excitation points into the vertical direction. Figure 22 depicts the surface current distribution over the helicopter at 7GHz

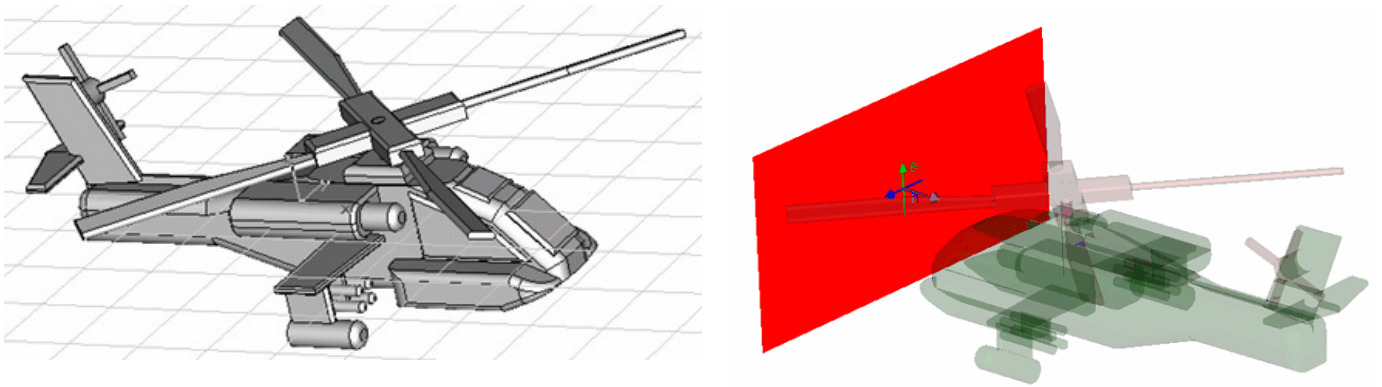


Figure 21 - The geometry of the helicopter and the plane wave excitation

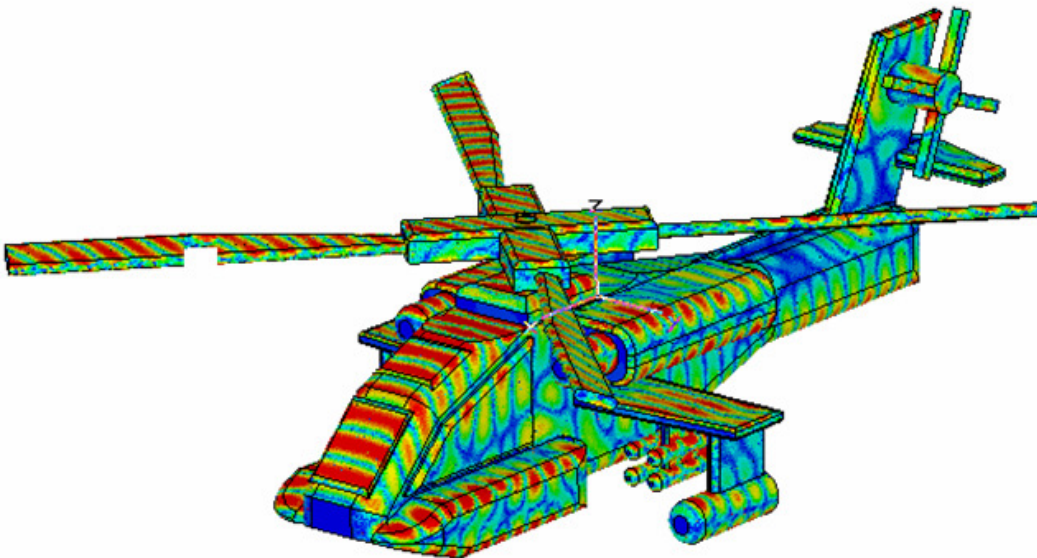


Figure 22- Surface current distribution at 7GHz

6. CONCLUSION

With the proliferation of electromagnetic solvers throughout microwave research and industry, their accuracy is becoming an issue of great practical importance. An overview of FIT and MoM (with the enhancement of MLFMM) numerical methods is presented along with a consistent number of examples covering different field of applications. It is demonstrated how FIT with the time domain solver is well suitable for broadband simulation and for complex geometry due to the non uniform hexahedral mesh enhanced by PBA and TST. Furthermore the possibility to implement FIT in both time and frequency domain allows validating the results by using two complete different mesh types: hexahedral and tetrahedral.

MoM is presented to be very powerful for large structure, in principle dominated by metal, although some results show the accuracy of the method for dielectric problems as well (dielectric sphere). From the present study it appears that FIT is very useful for the solution of a very broad band problem types, while MoM with MLFMM is reserved for more exclusive applications and large models $30-50\lambda$.

Acknowledgments

The authors would like to thanks J. Wang with CST of America for the simulation of the almond NASA and J. Eberhard for the useful discussions on the MoM method and for providing the helicopter model/results.

References

- [1] T. Weiland, "A discretization method for the solution of Maxwell's equations for six-component fields", *Electronics and Communication, (AEÜ)*, Vol. 31 (1977), p. 116.
- [2] T. Weiland, "Time Domain Electromagnetic Field Computation with Finite Difference Methods", *International Journal of Numerical Modelling*, Vol. 9, pp. 295-319 (1996).
- [3] B. Krietenstein, R. Schuhmann, P. Thoma and T. Weiland, "The Perfect Boundary Approximation technique facing the challenge of high precision field computation", *Proc. of the XIX International Linear Accelerator Conference (LINAC'98)*, Chicago, USA, 1998, pp. 860-862.
- [4] K.S. Yee, "Numerical Solution of Initial Boundary Value Problems Involving Maxwell's Equations in Isotropic Media", *IEEE, Antennas and Propagation* 14, 1966, pp.302-307.
- [5] V.Radisic, Y.Qian, R. Coccioli, T. Itoh, "Novel 2-D Photonic Bandgap Structure for Microstrip Lines", *IEEE Microwave and Guided Wave Letters*, vol.8, n.2, February 1998.
- [6] Abhari, G.V. Eleftheriades, "Metallo - dielectric electromagnetic band gap structures for suppression and isolation of parallel-plate noise in high speed circuits", *IEEE Trans. On Microwave Theory and Tech*, vol. 51, no. 6, pp. 1629-1639, June 2003.
- [7] G.Chen, K.L.Melde, "Cavity resonance suppression in power delivery systems using electromagnetic band gap structures", *IEEE Transaction on Advanced Packaging*, vol. 29, no. 1, pp. 21-30, February 2006.
- [8] S. Shahparnia, O. M. Ramahi, "Electromagnetic interference (EMI) and reduction from printed circuit boards (PCB) using electromagnetic bandgap structures", *IEEE Trans. Electromagnetic Comp*, vol. 46, no. 4, pp. 580-587, November 2004.
- [9] J.Choi, V.Govind, M. Swaminathan, "A novel electromagnetic band gap (EBG) structure for mixed signal system applications", *Proc. of IEEE Radio and Wireless*, Atlanta, Georgia, September 2004.

- [10] J.Choi, V. Govind, M. Swaminathan et Al., Noise suppression and isolation in mixed signal systems using alternative impedance electromagnetic bandgap (AI-EBG) structure”, accepted for *IEEE Trans. on Electromagnetic Compatibility*.
- [11] A.Ciccomancini Scogna, M.Schauer, “A Novel Electromagnetic Bandgap Structure for SSN Suppression in PWR/GND plane pairs”, in Proc. of ECTC 2007, Nevada, USA.
- [12] S.H.Hall, G. W.Hall, J.A.McCall, *High-Speed Digital System Design – A Handbook of Interconnect Theory and design Practises*, John Wiley & Sons, INC., New York, USA, 2000.R. F. Harrington, *Time-harmonic Electromagnetic Fields*, McGraw-Hill, 1961
- [13] K.Naishadham, T. Durak “Measurement-Based Closed-Form Modeling of Surface-Mounted RF Components”, *IEEE Trans. Microwave Theory Tech.*, vol. 50, no.10, pp. 2276-2286, October 2002.
- [14] G. Antonini, A Ciccomancini Scogna, A. Orlandi, “Equivalent circuit extraction for an SMA connector”, in *Proc. of PIERS 2003*, Pisa, Italy.
- [15] R.F. Harrington, “Field Computation by Moment Methods”, The Macmillan Co., New York, 1968.
- [16] G.S. Smith, “An Introduction to Classical Electromagnetic Radiaton”, Cambridge: Cambridge University Press, 1997.
- [17] Eberhard, J.P. “The Integral Equation Solver”, Proceedings of the CST Field Training 2006, Oct. 8th-11th 2006, Darmstadt, Germany.
- [18] Davidson, D.B., “Computational Electromagnetics for RF and Microwave Engineering”, Cambridge: Cambridge University Press, 2005.
- [19] Ishimaru, A., “Electromagnetic Wave Propagation, Radiation, and Scattering”, New Yersey: Prentice-Hall, Inc., 1991
- [20] Hubing, T.H., “Survey of Numerical Electromagnetic Modeling Techniques” Internal Report nr TR91-1-001.3, University of Missouri-Rolla, 1991 (<http://www.emclab.umar.edu/pdf/TR91-1-001.pdf>)
- [21] Coifman, R, Rokhlin, V and Wandzura, S, “The Fast Multipole Method for the Wave Equation: A Pedestrian Prescription” *IEEE Antennas and Propagation Magazine*, vol. 35, no. 3, Jun. 1993, pp. 7–12.
- [22] R. F. Harrington, *Time-harmonic Electromagnetic Fields*, McGraw-Hill, 1961
- [23] Ali E. Yilmaz, J.Ming Jin, E. Michielssen, “Time Domain Adaptive Integral Method for Surface Integral Equations”, *IEEE Trans. on Antennas and Propag.*, vol.52, n.10, October 2004, pag. 2692-2708.

Exact Radiation by Isorefractive Slotted Elliptic Cylindrical Antenna

A-K. Hamid

Department of Electrical & Computer Engineering
University of Sharjah
P.O. Box 27272, Sharjah, United Arab Emirates
akhamid@sharjah.ac.ae

M.I. Hussein

Department of Electrical Engineering
United Arab Emirates University
P.O. Box 17555, Al-Ain, United Arab Emirates
MIHussein@uaeu.ac.ae

M. Hamid

Department of Electrical and Computer Engineering
University of South Alabama
Mobile, Alabama 36688, U.S.A.
email: mhamid@usouthal.edu

Abstract:

Exact solution of the electromagnetic radiation from a conducting slotted elliptical cylinder coated by an isorefractive material derived using the separation of variables technique. The fields inside and outside the dielectric layer are expressed in terms of Mathieu functions. No matrix inversion is required after obtaining exact expressions for the radiated field expansion coefficients by imposing the appropriate boundary conditions. Numerical results are plotted for the radiation pattern, aperture conductance and antenna gain. The results show that a slotted antenna coated with isorefractive material has more directive beam and lower side-lobes compared to that coated with conventional dielectric material of comparable physical dimensions.

1. Introduction

Radiation properties of an axially slotted antenna are very important in communications and airplane industries. Numerous authors in the literature have investigated the radiation by dielectric coated slotted circular and elliptical cylinders. For example, Hurd [1] studied the radiation pattern of a dielectric axially-slotted cylinder. The external admittance of an axial slot on a dielectric coated metal cylinder was investigated by Knop [2]. Shafai [3] obtained the radiation properties of an axial slotted antenna coated with a homogenous material. Wong [4,5] investigated the radiation properties of slotted cylinder of elliptical cross section while Richmond [6] studied the radiation from an axial slot antenna on a dielectric- coated elliptic cylinder. The analysis was later extended to the radiation by axial slots on a dielectric coated nonconfocal conducting elliptic cylinder by Ragheb [7]. Hussein and Hamid [8] studied the radiation by N axially slotted cylinders of elliptical cross section coated with a lossy dielectric material.

Recently, Hamid investigated the radiation characteristics of slotted circular or elliptical cylinder coated by lossy and lossless metamaterials [9-10].

Lately, materials possessing both lossy and lossless metamaterials have gained considerable attention by many researches [11-26]. Thus a new artificial class of materials with interesting electromagnetic properties has been recently introduced. Two media separated by an interface are called isorefractive (IR) if they have the same refractive index. Such a relation is maintained when the permittivity and permeability of the two media obey

$$\mu_1 \varepsilon_1 = \mu_2 \varepsilon_2 \quad (1)$$

So that the propagation constant k and the wavelength λ are the same in both media, where

$$k = \frac{2\pi}{\lambda} = \omega \sqrt{\varepsilon_i \mu_i}, \quad i = 1, 2 \quad (2)$$

In addition, the two media have different intrinsic impedances, i.e.

$$Z_i = \sqrt{\frac{\mu_i}{\varepsilon_i}}, \quad i = 1, 2 \quad (3)$$

In this paper, a theoretical analysis based on a boundary value solution for the case of antenna radiation by an axial slot on a conducting circular or elliptical cylinder coated by an IR metamaterial is presented. The fields inside and outside the IR coating are expressed in terms of radial and angular Mathieu functions. The IR metamaterial elliptic layer allows an exact solution as the boundary conditions lead to one-to-one matching between the field modes on either side of the interface. Thus there is no need for matrix inversion since new expressions are obtained for the radiated field expansion coefficients. Numerical results are presented for the radiation pattern, aperture

conductance and antenna gain vs coating thickness as well as compared with uncoated, conventionally dielectric-coated and isorefractive-coated antenna.

2. Problem Formulation

Fig. 1 illustrates the geometry of the problem. The structure is assumed to be infinite along the z -axis. The symbols a_c and b_c correspond to the semi-major and semi-minor axes of the conducting cylinder, respectively, while the symbols a and b are semi-major and semi-minor axes of the dielectric coating. The elliptical coordinate system (u, v, z) is defined in terms of the Cartesian coordinate system (x, y, z) by $x = F \cosh(u) \cos(v)$ and $y = F \sinh(u) \sin(v)$, where F is the semifocal length of the elliptical cross section.

The electric fields outside the dielectric layer (region I) for $(\xi > \xi_1)$ and inside the dielectric layer (region II) for $\xi < \xi_1$ can be expressed in terms of Mathieu functions as follows

$$E_z^I = \sum_{m=0}^{\infty} C_{em} R_{em}^{(4)}(c, \xi) S_{em}(c, \eta) + \sum_{m=1}^{\infty} C_{om} R_{om}^{(4)}(c, \xi) S_{om}(c, \eta) \quad (4)$$

$$E_z^{II} = \sum_{m=0}^{\infty} [A_{em} R_{em}^{(1)}(c, \xi) + B_{em} R_{em}^{(2)}(c, \xi)] S_{em}(c, \eta) + \sum_{m=1}^{\infty} [A_{om} R_{om}^{(1)}(c, \xi) + B_{om} R_{om}^{(2)}(c, \xi)] S_{om}(c, \eta) \quad (5)$$

where A_{om} , B_{om} and C_{om} are the unknown expansion coefficients, $R_{em}^{(1)}$, $R_{em}^{(2)}$ and $R_{em}^{(4)}$ are the even and odd modified Mathieu functions of the first, second and fourth kinds, respectively. It should be noted that, $\xi = \cosh u$, $\eta = \cos v$ while $c = kF$. The magnetic field components inside and outside the dielectric layer can be obtained using Maxwell's equations as

$$H_v^I = \frac{-j}{\omega \mu_1 h} \left\{ \sum_{m=0}^{\infty} C_{em} R_{em}^{(4)'}(c, \xi) S_{em}(c, \eta) + \sum_{m=1}^{\infty} C_{om} R_{om}^{(4)'}(c, \xi) S_{om}(c, \eta) \right\} \quad (6)$$

$$H_v^H = \frac{-j}{\omega\mu_2 h} \left\{ \sum_{m=0}^{\infty} [A_{em} R_{em}^{(1)'}(c, \xi) + B_{em} R_{em}^{(2)'}(c, \xi)] S_{em}(c, \eta) + \sum_{m=1}^{\infty} [A_{om} R_{om}^{(1)'}(c, \xi) + B_{om} R_{om}^{(2)'}(c, \xi)] S_{om}(c, \eta) \right\} \quad (7)$$

where $h = F\sqrt{\cosh^2 u - \cos^2 v}$. The prime in equations (6) and (7) denotes derivative with respect to u while μ_1 and μ_2 are the permeabilities of regions 1 and 2, respectively.

We require the tangential components of the electric and magnetic fields to be continuous across the interface at $\xi = \xi_1$. In region (II), we require also that the tangential electric field on the conducting surface ($\xi = \xi_c$) must vanish except at the slot location. Enforcing these boundary conditions with the help of the orthogonality property of the angular Mathieu functions, we obtain an exact expression of the radiated field as

$$C_{em}^{om} = \frac{F_{em}^{om}}{N_{em}^{om}(c)} \left[\frac{P_{em}^{om}(\xi_1, \xi_c) \frac{R_{em}^{(2)}(c, \xi_1)}{om} - \frac{R_{em}'^{(2)}(c, \xi_1)}{om}}{\frac{R_{em}^{(2)}(c, \xi_c)}{om} - \frac{R_{em}^{(2)}(c, \xi_c)}{om}} \right] \quad (8)$$

$$\left[\frac{P_{em}^{om}(\xi_1, \xi_c) R_{em}^{(4)}(c, \xi_1) - \frac{\mu_2}{\mu_1} R_{em}'^{(4)}(c, \xi_1)}{om} \right]$$

Where

$$P_{em}^{om}(\xi_1, \xi_c) = \frac{R_{em}^{(1)'}(c, \xi_1) R_{em}^{(2)}(c, \xi_c) - R_{em}^{(1)}(c, \xi_c) R_{em}'^{(2)}(c, \xi_1)}{om} \quad (9)$$

$$\frac{R_{em}^{(1)}(c, \xi_1) R_{em}^{(2)}(c, \xi_c) - R_{em}^{(1)}(c, \xi_c) R_{em}^{(2)}(c, \xi_1)}{om}$$

$$F_{en} = E_o \sum_k D_e^k(c, n) \int_{v_1}^{v_2} \cos[\pi(v - v_0)/(2\alpha)] \cos(kv) dv \quad (10)$$

$$F_{on} = E_o \sum_k D_o^k(c, n) \int_{v_1}^{v_2} \cos[\pi(v - v_0)/(2\alpha)] \sin(kv) dv \quad (11)$$

$$\nu_0 = (\nu_1 + \nu_2)/2 \quad (12)$$

$$\alpha = (\nu_2 - \nu_1)/2 \quad (13)$$

$$N_{om}(c) = \int_0^{2\pi} [S_{om}(c, \eta)]^2 d\eta \quad (14)$$

and D_o^k are the Fourier series coefficients [27].

3. Numerical Results

Once the unknown expansion coefficients are obtained, quantities of interest such as far field radiation pattern, antenna gain and aperture conductance can be computed. The far field expression of the antenna can be expressed as

$$E_z^I(\rho, \phi) = \sqrt{\frac{j}{k\rho}} e^{-jk\rho} \left[\sum_{m=0}^{\infty} j^m C_{em} S_{em}(c, \cos \phi) + \sum_{m=1}^{\infty} j^m C_{om} S_{om}(c, \cos \phi) \right] \quad (15)$$

where ρ and ϕ denote the polar coordinates in the circular cylindrical system. The antenna gain may be expressed as

$$G(\phi) = \frac{1}{Z_1 k \rho} \left[\left| \sum_{m=0}^{\infty} j^m C_{em} S_{em}(c, \cos \phi) \right|^2 + \left| \sum_{m=1}^{\infty} j^m C_{om} S_{om}(c, \cos \phi) \right|^2 \right] \quad (16)$$

where Z_1 is the intrinsic impedance of region I (in this case it is taken to be free space).

The aperture conductance per unit length of the slot antenna is defined as

$$G_a = 2\pi\rho \frac{S_{av}}{|E_0|^2} \quad (17)$$

where S_{av} is the average power density averaged over an imaginary cylinder of radius ρ and is given by

$$S_{av} = \frac{1}{2\pi Z_1 k \rho} \left[\sum_{m=0}^{\infty} |C_{em}| N_{em}(c) + \sum_{m=1}^{\infty} |C_{om}| N_{om}(c) \right] \quad (18)$$

The geometrical parameters used in obtaining the numerical results are $a_c = \lambda$, $b_c = \lambda/2$, $b = b_c + t$, where t is the coating thickness, $\nu_0 = 90^\circ$ and $\alpha = 2.8657^\circ$. Figure 2 shows the numerical results for the radiation pattern (gain versus ϕ) obtained for the uncoated antenna and is presented by solid line for comparison ($\epsilon_r = 1, \mu_r = 1$). The results for the antenna coated with conventional dielectric material are presented by dashed line ($\epsilon_r = 4, \mu_r = 1$). The results for the antenna coated with isorefractiare material presented by dotted line ($\epsilon_r = 4, \mu_r = 1/4$) for dielectric thickness $t = 0.15\lambda$. It can be seen that the IR coating makes the beam sharper and more directive with lower side-lobes (of about -40 dB at -90 and 270 degrees) when compared with the conventional dielectric material coating. This may be due to the fact that the radiated field in the IR layer does not suffer reflection since the wave number is the same in all regions. Fig. 3 is similar to Fig. 2 except the coating thickness is increased to 0.25λ . It can be seen that the conventional dielectric coating has diverged the antenna beam while the isorefractive material coating has reduced the side-lobes by 20 dB when it is compared with the uncoated antenna and by 40 dB when it is compared with the conventional dielectric coated antenna especially at -90 and 270 degrees. It is also worth mentioning the pattern of the uncoated and coated antenna with IR material looks like a band pass filter while the conventional coated antenna losses this important feature.

The gain versus electrical coating thickness for a single slotted elliptical antenna with the same geometrical parameters used in Fig. 2 is displayed in Fig. 4. The gain is evaluated at $\phi = 90^\circ$ since the slot is centered at $\nu = 90^\circ$ where the gain is expected to be maximum. For very small coating thickness, the conventional and IR coatings have the same effect on the gain. As t becomes greater than 0.05λ , IR coating increases the

antenna gain when compared with the conventional coating until the thickness becomes 0.275λ . Further, the presence of surface waves in the case of conventional coating starts to disappear in the case of IR coating for higher values of electrical thickness.

The aperture conductance for conventional and IR coatings is shown in Fig. 5 for an elliptical antenna with the same geometrical parameters used in Fig. 2. The antenna appears to have higher conductance values for IR coating thicknesses greater than 0.2λ , and lower conductance values for t less than 0.2λ when compared with conventional dielectric coating.

4. Conclusions

Exact radiation from a slot on a conducting elliptical cylinder coated with IR concentric layer was obtained using the boundary value technique with no matrix inversion required. The application of the boundary conditions has led to a one-to-one matching between the field modes on either side of the interface, and thus exact expressions were obtained for the radiation expansion coefficients. Finally, the IR coating may be used to enhance the gain and reduce the side-lobes of slotted antenna over a certain coating range.

References

- [1] R. A. Hurd, "Radiation patterns of a dielectric coated axially slotted cylinder," *Canadian J. Phys.*, vol. 34, pp. 638-642, July 1956.
- [2] C. M. Knop, "External admittance of an axial slot on a dielectric coated metal cylinder," *Radio Sci.*, vol. 3, pp. 803-818, Aug. 1968.
- [3] L. Shafai, "Radiation from an axial slot antenna coated with a homogenous material," *Canadian J. Phys.*, vol. 50, no. 23, 1972.

- [4] J. Y. Wong, "Radiation pattern of slotted elliptic cylinder antenna," *IEEE Trans. Antennas Propagat.*, vol. AP-3, pp. 200-203, Oct. 1955.
- [5] J. Y. Wong, "Radiation conductance of axial and transverse slots in cylinders of elliptical cross section," *Proc. IRE*, vol. 41, pp. 1172-1177, Sept., 1953.
- [6] J. H. Richmond, "Axial slot antenna on dielectric coated elliptic cylinder," *IEEE Trans. Antennas Propagat.*, vol. AP-37, pp. 1235-1241, Oct. 1989.
- [7] H. A. Ragheb, A. Sebak, and L. Shafai, "Radiation by axial slots on dielectric coated nonconfocal conducting elliptic cylinder," *IEE Proc. Microw. Antennas Propagat.*, vol. 143, no. 2, pp. 124-130, April 1996.
- [8] M.I. Hussein, and A-K. Hamid, "Radiation characteristics of N axial slots on a conducting elliptical antenna coated by a lossy dielectric layer," *Canadian Journal of Physics*, vol. 82, no. 2, pp. 141-149, 2004.
- [9] A-K. Hamid, "Axially Slotted Antenna on a Circular or Elliptic Cylinder Coated With Metamaterials," *Progress In Electromagnetic Research (Series Book)*, PIER 51, page 329-341, 2005.
- [10] A-K. Hamid, "Study of Lossy Effects on the Characteristics of Axially Slotted Circular or Elliptical Cylindrical Antenna Coated with Metamaterials," *IEE Proc. on Microwaves, Antennas & Propagation*, 2005. In press.
- [11] R. Ruppin, "Extinction properties of a sphere with negative permittivity and permeability," *Solid State Communications*, vol. 116, pp. 411-415, 2000.
- [12] N. Engheta, "An idea for thin subwavelength cavity resonators using metamaterials with negative permittivity and permeability", *IEEE Antennas and Wireless Propagation Letters*, vol. 1, pages 10-3, 2002.

- [13]C. Li and Z. Shen, “Electromagnetic scattering by a conducting cylinder coated with metamaterials”, Progress in Electromagnetics Research, PIER 42, pp. 91-105, 2003.
- [14]D.R. Smith, S. Schultz, P. Markos, and C.M. Soukoulis, “ Determination of effective permittivity and permeability of metamaterials from reflection and transmission coefficients” , Physical Review B, vol. 65, pp. 195104-(1-5), 2004.
- [15]T. J. Cui, Z-C. Hao, X. Yin, W. Hong, and J.A. Kong, “Study of lossy effects on the propagation of propagating and evanescent waves in the left-handed materials,” Physics Letters, A 323, pp. 484-494, 2004.
- [16]P. L. E. Uslenghi, "Exact scattering by isorefractive bodies," IEEE Trans. AntennPropagat., vol. 45, pp. 1382-1385, Sept., 1997
- [17] D. Erricolo and P. L. E. Uslenghi, "Exact radiation for dipoles on metallic spheroids at the interface between isorefractive half-spaces", IEEE Trans. Antenna Propagat, vol. 53, pp. 3974-3981, Dec 2005.
- [18]D. Erricolo and P.L.E. Uslenghi , "Exact radiation and scattering for an elliptic metal cylinder at the interface between isorefractive half-spaces", IEEE Trans. Antenna Propgat., vol. 52, No. 9, pp. 2214-2225, Sept. 2004.
- [19] P. L. E. Uslenghi, "Exact penetration, radiation, and scattering for a slotted semielliptical channel filled with isorefractive material", IEEE Trans. Antenna Propgat, vol. 52, No. 6, pp. 1473-1480, June 2004.
- [20]V Lindell, "Image theory for ved above a half-space of Veselago medium," Microwave and Optical Technology Letters, vol. 44, No. 2, pp. 185-190, Jan 20, 2005
- [21] S. Caorsind M. Pastorino, "Scattering by multilayer isorefractive elliptic cylinders", IEEE Trans. Antenna Propgat, vol. 52, No. 1, pp. 189-196, Jan 2004.
- [22] J. S. Tyo, "A class of artificial materials isorefractive with free space" IEEE Trans. Antenna Propgat., vol. 51, No. 5, pp. 1093-1099, May 2003.

- [23]S. A. Tretyakov , S.I. Maslovski, A.A. Sochava AA, et al.,”The influence of complex material coverings on the quality factor of simple radiating systems” IEEE Trans Antenna Propagat., vol. 53, No. 3, pp. 965-970, March 2005.
- [24] N. Engheta and R. Ziolkowski, "A positive future for double-negative metamaterials”, IEEE Trans. Microwave Theory Techn., vol. 53, No. 4, p.1535, 2005.
- [25]E. Shamonina and L. Solymar, “Properties of magnetically coupled metamaterial elements” J. Magnetism Magnetic Materials, vol. 300, No. 1, p. 38, 2006.
- [26]A. K. Hamid, “Multi-dielectric loaded axially slotted antenna on circular or elliptic cylinder J. Electromagnetic Waves and Applications, vol. 20, No. 9, pp. 1259-1271, 2006.
- [27] M. Morse, and HFeshbach, Methods of Theoretical Physics, vols. I and II, McGraw-Hill, New York 1953.

Acknowledgement

The authors wish to acknowledge the support provided by the University of Sharjah and the United Arab Emirates, UAE.

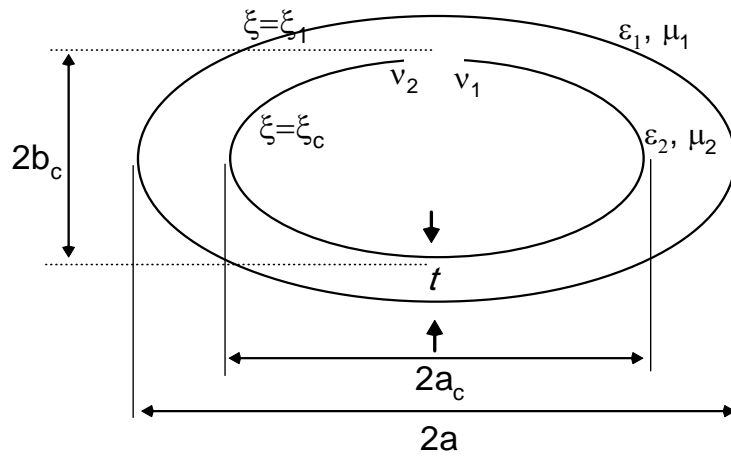


Figure 1: Geometry of axially Slotted antenna on elliptic cylinder with isorefractive layer

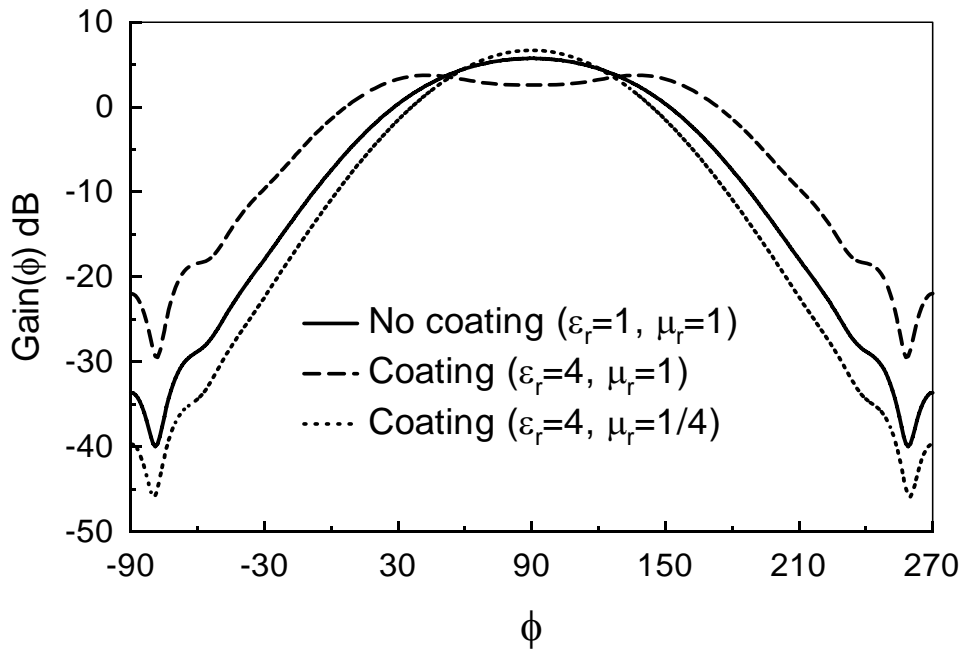


Figure 2: Radiation pattern for an axially slotted elliptic cylinder coated with different types of dielectric materials and coating thickness $t = 0.15\lambda$.

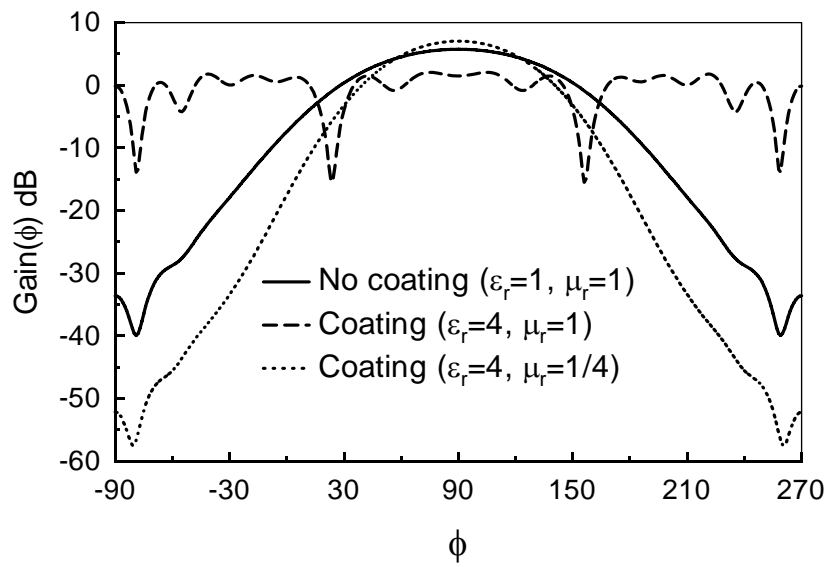


Figure 3: Radiation pattern for an axially slotted elliptic cylinder coated with different types of dielectric materials and coating thickness $t = 0.25\lambda$.

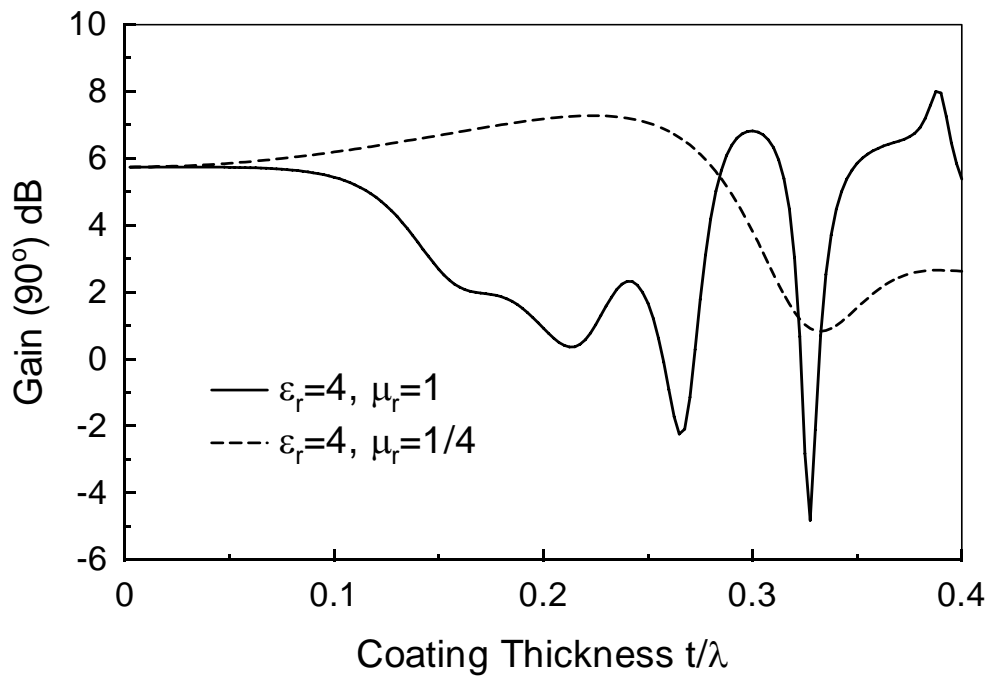


Figure 4: Gain versus coating thickness for an axially slotted elliptic cylinder coated with conventional and isorefractive dielectric materials.

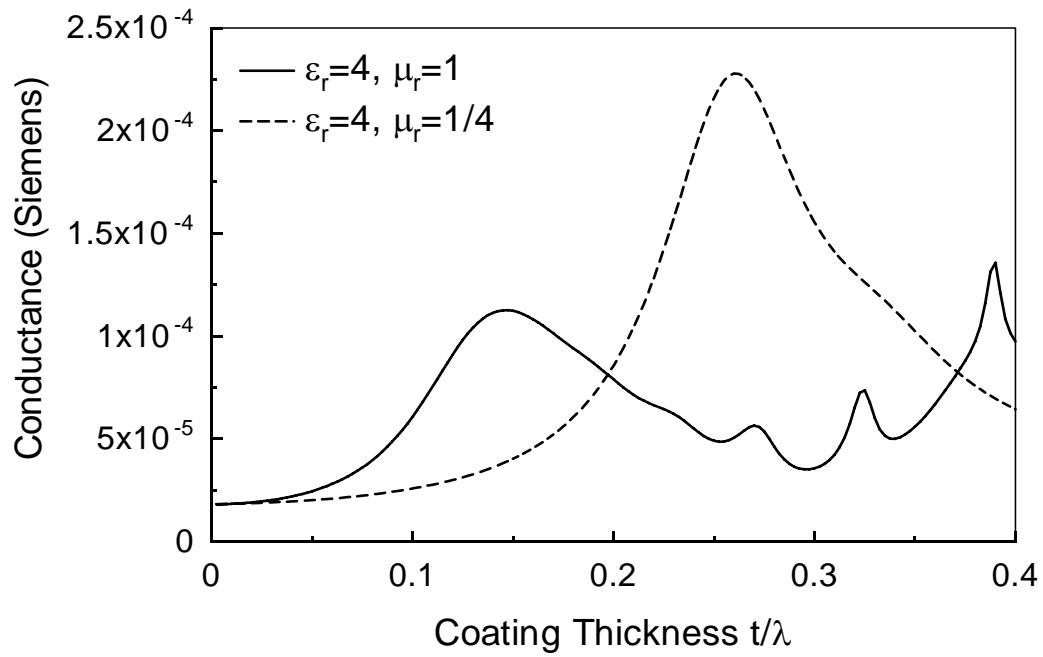


Figure 5: Aperture conductance versus coating thickness for an axially slotted elliptic cylinder coated with conventional and isorefractive materials.

ADVERTISING RATES		
	FEE	PRINTED SIZE
Full page	\$200	7.5" × 10.0"
1/2 page	\$100	7.5" × 4.7" or 3.5" × 10.0"
1/4 page	\$50	3.5" × 4.7"
<p>All ads must be camera ready copy.</p> <p>Ad deadlines are same as Newsletter copy deadlines.</p> <p>Place ads with Bruce Archambeault, barch@us.ibm.com. The editor reserves the right to reject ads.</p>		

DEADLINE FOR THE SUBMISSION OF ARTICLES	
Issue	Copy Deadline
March	February 1
July	June 1
November	October 1

For the **ACES NEWSLETTER**, send copy to Bruce Archambeault in the following formats:

1. A PDF copy.
2. A MS Word (ver. 97 or higher) copy. If any software other than WORD has been used, contact the Managing Editor, Richard W. Adler **before** submitting a diskette, CD-R or electronic file.

Last Word

“A scientific truth does not triumph by convincing its opponents and making them see the light, but rather because its opponents eventually die and a new generation grows up that is familiar with it. “

Maxwell Planck